Check for updates

Enhanced structural and optical performance of the novel 3-[(5-amino-1-phenyl-1*H*-pyrazol-4-yl) carbonyl]-1-ethyl-4-hydroxyquinolin-2(1*H*)-one heterojunction: experimental and DFT modeling

Magdy A. Ibrahim[1] · **Al-Shimaa Badran**[1] · **Shimaa Abdel Halim**[1] · **N. Roushdy**[2] · **A. A. M. Farag**[3]

Abstract

This study successfully and cost-effectively synthesized a novel compound, 3-[(5-amino-1-phenyl-1*H*-pyrazol-4-yl)carbonyl]-1-ethyl-4-hydroxyquinolin-2(1*H*)-one (**APPQ, 4**), which displayed significant potential for various applications and yielded promising outcomes. Theoretical electronic absorption spectra in different media were acquired using the Coulomb-attenuating approach (CAM-B3LYP) and the Corrected Linear Response Polarizable Continuum Model (CLR) PCM. Employing CAM-B3LYP with the $6\text{-}311++G(d,p)$ level of DFT proved to be more accurate than alternative quantum chemical calculation methods, aligning well with the experimental data. Additionally, the CAM-B3LYP method using polarized split-valence $6\text{-}311++G(d,p)$ basis sets and CLR PCM in various solvents exhibited good agreement with the observed spectra. The high stability of **APPQ**, validated by the computed total energy and thermodynamic parameters at the same calculation level, surpassed that of anticipated structure **3**. The theoretically calculated chemical shift values (^{1}H and ^{13}C) and vibrational wavenumbers were strongly correlated with the experimental data. The **APPQ** thin films demonstrated a band gap energy of 2.3 eV through distinctive absorption edge measurement. Photoluminescence spectra exhibited characteristic emission peaks at approximately 580 nm. Current–voltage measurements on n-Si heterojunction devices with **APPQ** thin films revealed typical diode behavior. These **APPQ**-based devices showed attractive photovoltaic properties, including an open-circuit voltage of 0.62 V, a short-circuit current of 5.1×10^{-4} A/cm^2, and a maximum output power of 0.247 mW/cm^2. Overall, the investigated heterojunctions display appealing photophysical characteristics, encouraging advancements in photovoltaics.

Keywords Structural properties · DFT/TD-DFT, UV–vis spectrum · Photovoltaic applications

1 Introduction

Pyrans and fused pyrans possess remarkable biological properties including antimicrobial, antifungal, antitumor, anticoagulant, diuretic, spasmolytic, and anti-anaphylactic activity (Hussein et al. 2012). Moreover, 4*H*-pyrans play a crucial role as foundational components of a diverse range of natural products. Certain 2-amino-4H-pyrans are used as photoactive materials, pigments, and potentially biodegradable agrochemicals (Safari et al. 2012; Wang et al. 2011). In the field of medicinal chemistry, heterocyclic systems incorporating a quinoline nucleus hold significant importance, as they are prevalent substructures found in biologically active natural compounds. Among them, quinoline compounds featuring a pyranoquinoline core serve as the essential framework for various alkaloids such as flindersine, oricine, and surprisingly. These compounds exhibit a wide spectrum of biological effects, including anti-allergic, psychotropic, anti-inflammatory, and antibacterial activities (Safari et al. 2012; Wang et al. 2011; Romdhane and Jannet 2017). Some applications of pyrano[3,2-*c*] quinolines include the production of photovoltaic, optoelectronic, fluorescent, luminescent, semiconductor, and photodiode components (Soliman and Yahia 2020; Farag et al. 2019a; Abdel Halim and Ibrahim 2017).

Pyranoquinoline derivatives have gained attention owing to their favorable properties in various applications. They have demonstrated potential for use in nonlinear optical devices (Abdel Halim et al. 2023; Farag et al. 2020), medicine (Uppal et al. 2023), and other fields (Li et al. 2019; Chernyshev et al. 2022). These derivatives exhibit hygienic properties and bacteriolytic activities and show promise in areas such as allergy treatment, inflammation control, and AChE inhibition. They also serve as pharmacophores for the development of psychotropic drugs, treatments for sexually transmitted diseases, and anticancer therapies (Zaman et al. 2019; Asghari et al. 2014; Kantevari et al. 2011). Styryl-quinolines and Au(III) based-dithiolene complexes are effective materials for non-linear optical applications (Upadhyay and Shah 2019).

Quinoline derivatives are used as corrosion inhibitors for iron, whereas pyranopyrimidines with coumarin substituents have shown DNA gyrase inhibitory properties. Organic photovoltaics, known for their cost-effective fabrication and high-energy conversion capabilities, have been explored using novel organic photovoltaic devices. Pyranoquinolinone derivatives are particularly notable for their antitumor/antioxidant activities, protein-monitoring abilities, and potential in the synthesis of antifungal and antibacterial medications (Mostafa et al. 2023).

The nonlinear optical (NLO) effect is at the forefront of current research because pyranoquinolines and their derivatives are crucial for providing the essential functions of frequency shifting, optical modulation, optical switching, optical logic, and optical memory for emerging technologies in fields like telecommunications, signal processing, and optical interconnections (Farag et al. 2019b). As a density surface that simultaneously displays molecular size, shape, and electrostatic potential in terms of color grading, molecular electrostatic potential (MESP) mapped onto an electron is a very useful tool for analyzing the molecular structure and physiochemical characteristics of molecules like biomolecules and medications (Mostafa et al. 2017).

The photophysical, photovoltaic, and optoelectronic properties of some organic molecules were determined using the CAM-B3LYP/6-31G (d,p) level of DFT (Mehboob et al. 2022a, 2022). Modifications with end caps and π-conjugation led to an improvement in the optoelectronic properties of the designed molecules to be used as acceptors for high-efficiency organic solar cells (Mehboob et al. 2022a, 2022). The utilization of the

CAM-B3LYP method, coupled with the 6-311 + +G(d,p) level of DFT, yields more accurate data compared to alternative quantum chemical calculation methods when assessing experimental data. Furthermore, the CAM-B3LYP basis set was employed to theoretically analyze electronic absorption spectra in the gas phase (TD-DFT), utilizing polarized split-valence 6-311 + +G(d,p) basis sets. Additionally, the application of CLR-PCM in various solvents, namely DMF, acetone, butanol, dioxane, toluene, and xylene, demonstrates a robust agreement with the observed spectra, offering practical significance.

The motivation for this work lies in the comprehensive investigation of the synthesized compound's properties, showcasing its potential in various applications, particularly in the field of photovoltaics. The observed characteristics, both theoretical and experimental, contribute to the advancement and understanding of this novel compound.

The presented structure (**APPQ**, **4**) is classified as an organic semiconductor of small molecules, is specified as an π-conjugated nanostructure structure, and has a delocalization of electrons as well as a large extinction coefficient and good light gain. In this article, we present innovative methods for producing and characterizing thin films and powders of organic semiconductors (**APPQ**). To further investigate its optoelectronic characteristics, this functional structure was examined using various experimental methods and theoretical procedures. Density functional theory (DFT) was used to describe the structural and spectral characteristics and establish the relationship between the structure and characteristics. DFT is the best tool for this job in this situation. These calculations allow us to describe the applicability field and provide experimentally unavailable information. Owing to advancements in data processing, computations utilizing large-scale basis sets and associated experimental information have recently become achievable. Finally, the optical properties of absorption and photoluminescence of the **APPQ** were measured, and the suitability of the **APPQ**/n-Si heterojunction used for applications in the field of organic photovoltaic cells was confirmed and these molecules are related to the novel systems in literature (Mehboob et al. 2020, 2021, 2022; Hussain et al. 2020; Siddique et al. 2021a; Akram et al. 2021).

2 Experimental

2.1 Synthesis and characterization of APPQ

To obtain **APPQ**, a mixture of 6-ethyl-4,5-dioxo-5,6-dihydro-4*H*-pyrano[3,2-c]quinoline-3-carbonitrile (**1**) (0.80 g, 3 mmol) and phenylhydrazine (0.33 g, 3 mmol) in 30 mL of ethanol was refluxed for 45 min. Upon cooling, the resulting yellow powder was filtered and recrystallized using methanol. mp 268–269 °C, yield (0.86 g, 77%). IR (KBr, cm^{-1}): 3450 (OH), 3332, 3190 (NH$_2$), 3066 (CH$_{arom.}$), 2994, 2850 (CH$_{aliph.}$), 1675 (C=O$_{ketone}$), 1655 (C=O$_{quinolone}$), 1618 (C=N) and 1578 (C=C). ^{1}H NMR (DMSO-d_6, δ, 400 MHz): 1.21 (t, 3H, J=6.4 Hz, CH$_2$*CH$_3$*), 4.27 (q, 2H, J=6.4 Hz, *CH$_2$*CH$_3$), 6.43 (bs, 2H, NH$_2$ exchangeable with D$_2$O), 6.90 (d, 1H, J=7.6 Hz, Ar–H), 7.20 (t, 1H, J=7.2 Hz, Ar–H), 7.43 (t, 1H, J=7.6 Hz, Ar–H), 7.55–7.59 (m, 3H, Ar–H), 7.61 (d, 1H, J=7.6 Hz, Ar–H), 7.79 (t, 1H, J=8.0 Hz, Ar–H), 8.23 (d, 1H, J=7.2 Hz, Ar–H), 8.32 (s, 1H, H-3$_{pyrazole}$). ^{13}C NMR (DMSO-d_6, δ, 100 MHz): 12.2 (CH$_3$), 38.2 (CH$_2$), 94.3 (C-4$_{pyrazole}$), 111.5 (C-3$_{quinoline}$), 118.1, 120.5, 121.2, 123.6, 126.4, 127.0, 128.2, 129.5, 135.3, 139.0 (12Ar-C), 140,6 (C-3$_{pyrazole}$), 153.5 (C-5$_{pyrazole}$), 161.3 (C–OH), 171.8 (C-2$_{quinoline}$ as C=O), 191.5 (C=O). Mass spectrum, m/z (I_r %): 374 (M$^{+·}$, 65), 343 (27), 317 (16), 304 (9), 216 (8), 190 (7), 160 (10), 132 (22), 80 (31), 77 (20), 64 (100).

Anal. Calcd for $C_{21}H_{18}N_4O_3$ (374.40): C, 67.37; H, 4.85; N, 14.96%. Found: C, 67.10; H, 4.60; N, 14.75%.

Melting points were determined using a digital Stuart SMP3 apparatus. Infrared spectra were obtained using FTIR Nicolet IS10 and Perkin-Elmer 293 spectrophotometers with KBr disks as the medium. ^{1}H NMR (300 MHz) and ^{13}C NMR (75 MHz) spectra were recorded on a Mercury-300BB instrument using DMSO-d6 as the solvent and TMS (δ) as the internal standard. Mass spectra were acquired using a GC-2010 Shimadzu Gas chromatography instrument mass spectrometer (70 eV). Elemental microanalyses were performed using a Perkin–Elmer CHN-2400 analyzer.

2.2 Computational details

In this study, computational calculations were performed using the Gaussian 09 software package (Frisch et al. 2009), and the obtained results were analyzed using the GaussView 05 molecular visualization program (Frisch et al. 2009). To determine the optimized geometrical parameters, vibrational frequencies, UV–Vis spectra, electronic transitions, and electronic characteristics such as HOMO–LUMO energies for **APPQ**, Density Functional Theory (DFT) (Shahab et al. 2015) was employed using the B3LYP hybrid functional (Yanai et al. 2004). The B3LYP functional combines the Lee–Yang–Parr correlation functional (LYP) with Beck's three-parameter hybrid exchange functional (B3), and the Coulomb Attenuating Method (CAM-B3LYP) was utilized (Lee et al. 1988). For a more accurate representation of polar bonding in molecules, the basis set 6-311 + + G(d,p) basis set with 'd' polarization functions on heavy atoms and 'p' polarization functions on hydrogen atoms was used (Petersson and Allaham 1991). NMR chemical shifts were estimated using the gauge-including atomic orbital (GIAO) approach (Wolinski et al. 1990), employing the same level of theory. Donor–acceptor interactions on the NBO basis were evaluated using the second-order Fock matrix (Sarafran et al. 2007). Geometrical optimization, FMO, MEP, etc. in the context of organic compounds involves finding the most energetically favorable arrangement of atoms in a molecule. This optimization is crucial for understanding the chemical and physical properties of a compound as discussed in the literature (Ans et al. 2019a, 2019b, 2019c, 2019d, 2019e, 2020a, 2020b, 2022; Siddique et al. 2020, 2021, 2022).

2.3 Preparation and characterizations of APPQ films

APPQ thin films were fabricated on different substrates via vacuum thermal evaporation. Morphological analysis was conducted using a JEOL-JSM-636 OLA scanning electron microscope, and the optical properties were assessed using a JASCO–670 spectrophotometer. To investigate the characteristics of the hybrid heterostructure based on **APPQ**, the current–voltage measurements were conducted under both dark conditions and varying light intensities using a high-impedance Keithley 2635 A.

3 Results and discussion

3.1 Synthesis and molecular structure characterization

A new compound, 3-[(5-amino-1-phenyl-1H-pyrazol-4-yl)carbonyl]-1-ethyl-4-hydroxyquinolin-2(1H)-one (**APPQ**, 2), was synthesized by treating
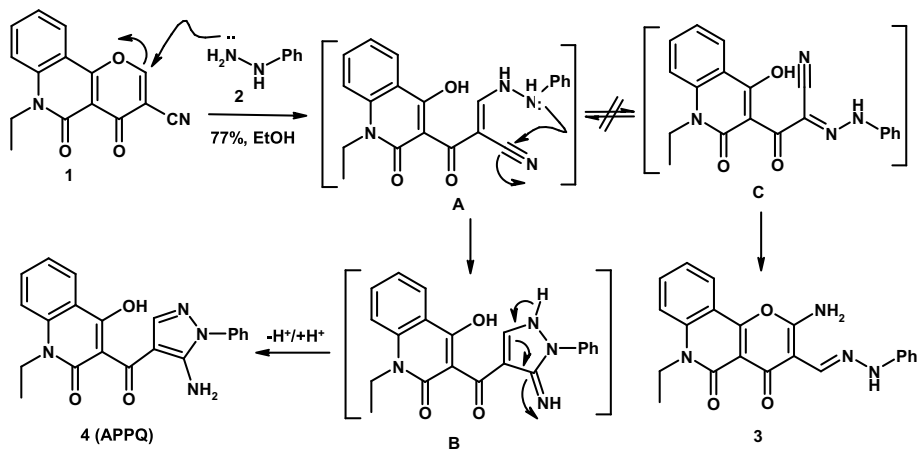
Scheme 1 Formation of the novel **APPQ, 4**

6-ethyl-4,5-dioxo-5,6-dihydro-4H-pyrano[3,2-c]quinoline-3-carbonitrile (**1**) (Ibrahim et al. 2013) with phenylhydrazine in boiling ethanol as shown in Scheme 1. The formation of compound **4** was proposed to involve nucleophilic attack at the C-2 position of the γ-pyrone ring, leading to the formation of intermediate **A**. Subsequently, pyrazole ring closure occurred through the addition of the amino group to the cyano group (intermediate **B**), accompanied by proton transfer. The formation of another potential product, compound **3**, resulting from the addition of a hydroxyl group to the cyano functional group (intermediate **C**), was ruled out based on spectral analysis. Computational analysis of compounds **3** and **4** further supports this proposed mechanism.

To obtain **APPQ**, a mixture of 6-ethyl-4,5-dioxo-5,6-dihydro-4H-pyrano[3,2-c]quinoline-3-carbonitrile (**1**) (0.80 g, 3 mmol) and phenylhydrazine (0.33 g, 3 mmol) in 30 mL of ethanol was refluxed for 45 min. Upon cooling, the resulting yellow powder was filtered and recrystallized using methanol. mp 268–269 °C, yield (0.86 g, 77%). IR (KBr, cm^{-1}): 3450 (OH), 3332, 3190 (NH$_2$), 3066 (CH$_{arom.}$), 2994, 2850 (CH$_{aliph.}$), 1675 (C=O$_{ketone}$), 1655 (C=O$_{quinolone}$), 1618 (C=N) and 1578 (C=C). ^{1}H NMR (DMSO-d_6, δ, 400 MHz): 1.21 (t, 3H, $J = 6.4$ Hz, CH$_2$CH$_3$), 4.27 (q, 2H, $J = 6.4$ Hz, CH$_2$CH$_3$), 6.43 (bs, 2H, NH$_2$ exchangeable with D$_2$O), 6.90 (d, 1H, $J = 7.6$ Hz, Ar–H), 7.20 (t, 1H, $J = 7.2$ Hz, Ar–H), 7.43 (t, 1H, $J = 7.6$ Hz, Ar–H), 7.55–7.59 (m, 3H, Ar–H), 7.61 (d, 1H, $J = 7.6$ Hz, Ar–H), 7.79 (t, 1H, $J = 8.0$ Hz, Ar–H), 8.23 (d, 1H, $J = 7.2$ Hz, Ar–H), 8.32 (s, 1H, H-3$_{pyrazole}$). ^{13}C NMR (DMSO-d_6, δ, 100 MHz): 12.2 (CH$_3$), 38.2 (CH$_2$), 94.3 (C-4$_{pyrazole}$), 111.5 (C-3$_{quinoline}$), 118.1, 120.5, 121.2, 123.6, 126.4, 127.0, 128.2, 129.5, 135.3, 139.0 (12Ar-C), 140,6 (C-3$_{pyrazole}$), 153.5 (C-5$_{pyrazole}$), 161.3 (C–OH), 171.8 (C-2$_{quinoline}$ as C=O), 191.5 (C=O). Mass spectrum, m/z (I_r %): 374 (M$^{+\cdot}$, 65), 343 (27), 317 (16), 304 (9), 216 (8), 190 (7), 160 (10), 132 (22), 80 (31), 77 (20), 64 (100). Anal. Calcd for C$_{21}$H$_{18}$N$_4$O$_3$ (374.40): C, 67.37; H, 4.85; N, 14.96%. Found: C, 67.10; H, 4.60; N, 14.75%.

Computational analysis was performed to support the formation mechanism of compound **4** (**APPQ**) and to reject the suggestion of another product (compound **3**). The proposed mechanism in Scheme 1 was confirmed through theoretical calculations (Fig. 1), which revealed that the charge density at C-2 was lower than that of the cyano carbon. Consequently, C-2 becomes a carbon-deficient site that is readily attacked by a nucleophilic
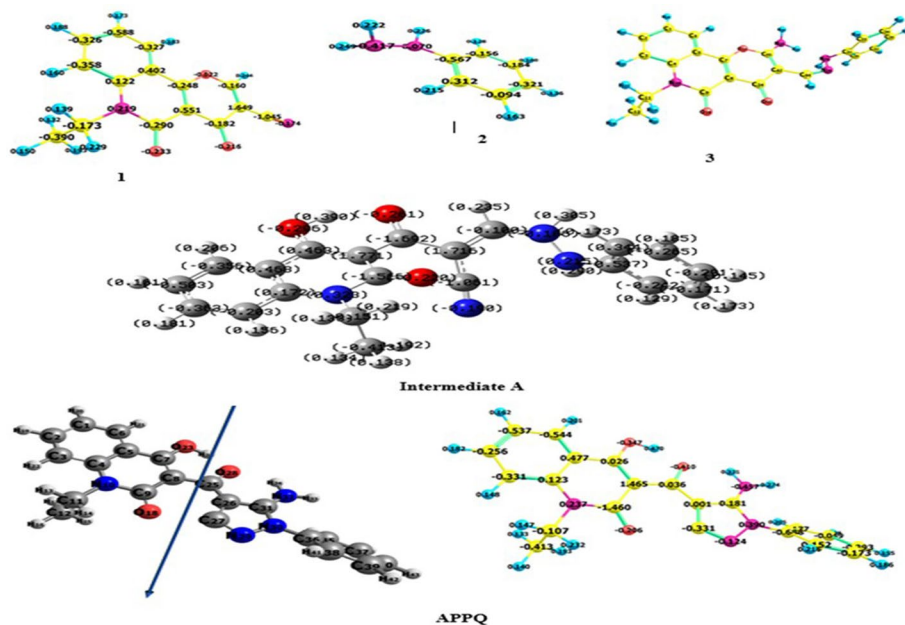
Fig. 1 The optimized structure of compounds **1, 2, 3**, intermediate **A** and the product (**APPQ**). Natural charge of compounds intermediate **A** and (**APPQ**)

reagent (phenyl hydrazine). Moreover, although the NH group in the optimized structure of intermediate **A** exhibits a lower electron density (0.215) than the OH group (−0.296), the reduced electron density in the NH group can be attributed to the delocalization of the lone pair of electrons over the benzene ring. Another factor influencing the nucleophilic addition of the NH group to the nitrile group in the reaction mechanism is the stabilization energy of the resulting product, **APPQ** (Scheme 1). Consequently, intermediate **A** favors the route to intermediate **B,** and subsequently the final product (**APPQ**) more preferable than the route to intermediate **C** and excluded product **3**. The computational results obtained for **APPQ** demonstrated its higher stability and reactivity compared to compound **3**, with values of (0.2693 eV and 6.2074 kcal/mol). Additionally, **APPQ** exhibits lower hardness and higher softness, along with greater electrophilicity, than compound **3**. Therefore, **APPQ** was more stable and reactive than compound **3**.

3.2 Chemical reactivity characteristics

A key factor in Gaussian calculations is the estimation of the HOMO (−donor) and LUMO (−acceptor) energies, and how these energies overlap has a vital impact on the occurrence of various reactions (Yousef et al. 2012; Liu et al. 2012). The most significant stability metric for demonstrating the chemical reactivity and kinetic stability of molecules is the energy gap (E_{LUMO}–E_{HOMO}) (Govindarajan et al. 2012). The chemical reactivity and site selectivity of the molecular systems were explained by the DFT approach. The global reactivity descriptors, as described in the literature (Yanai et al. 2004, Lee et al. 1988) and presented in Table 1, offer a valuable tool for comparing

the reactivity of the product **APPQ** with other molecules under study. These descriptors encompass various factors, as stated in detail in the literature, and are summarized in Table 1. These descriptors were calculated for reactants **1** and **2**, as well as for the isolated product **APPQ** (**4**), and another anticipated product **3**, utilizing the energies of the frontier molecular orbitals (E_{LUMO}, E_{HOMO}), as shown in Table 1 and Fig. 2. The electrophilicity index gauges the amount of energy needed to stabilize a chemical system after transferring an additional electronic charge (ΔN_{max}) from its surroundings. The direction of charge transfer from nucleophiles to electrophiles is dictated by the electronic chemical potentials of the reactant molecules. Consequently, when a molecule accepts an electronic charge, its energy decreases, leading to a negative electronic chemical potential. Electrophilic charge transfer (ECT) is defined as the difference between the ΔN_{max} values of interacting molecules as present in the following equation: $ECT = (\Delta N_{max})_1 - (\Delta N_{max})_2$. The electronic charge (ΔN_{max}) was calculated for reactant molecules which are 6-ethyl-4,5-dioxo-5,6-dihydro-4*H*-pyrano[3,2-*c*]quinoline-3-carbonitrile (**1**) and phenyl hydrazine (**2**), as well as for the final product **4**. The calculated ECT value for the reactant molecules was 1.124809, indicating the transfer of electron charge from reagent **2** to substrate **1**. As a result, molecule **1** can be identified as a global electrophile (electron acceptor), whereas molecule **2** acts as a global nucleophile (electron donor).

In contrast to compound **1**, which exhibits a low chemical potential and high electrophilicity index, compound **2** displays a low electrophilicity index and high chemical potential, indicating its nucleophilic activity (Table 1). The product **4** (**APPQ**) possesses a higher electrophilicity index ($\omega = 4.433508$ eV) than reactant molecule **2** ($\omega = 1.8786$ eV), indicating that molecule **4** (**APPQ**) is a stronger electrophile than molecule **2**.

Further, a good nucleophile is characterized by low values of (ω), while a good electrophile is characterized by high values of (ω) (hydroxynaphthalen-2-yl)methylene)-N-(pyridin-2-yl) hydrazinecarbothioamide and its Mn(II) Ni(II) 2012). The importance of hardness (η) and softness (S) is to measure molecular stability and reactivity. The more polarized and reactive molecules have a small energy gap and are known as soft molecules. Thus, compound **APPQ** ($S = 0.513258$ eV^{-1}) is more soft than other compounds. While compound **3** has the most hardness. Additionally, Pauling defined electronegativity as an atom's capacity to draw an electron to itself within a molecule (Pauling et al. 1960). So, compound **1** has more electronegativity than other compounds. Table 1 shows the chemical softness and other factors of **APPQ** compared to those with similar structures. The values of these factors for **APPQ** were very close to those reported for similar structures, with only a small margin of error from the calculations. This indicates that the results are reliable and accurate (Wolinski et al. 1990; Sarafran et al. 2007; Ans et al. 2019a; 2020).

3.3 Molecular geometry of APPQ

The structure of **APPQ** was identified using density functional theory and the B3LYP and CAM-B3LYP functional calculations. The CAM-B3LYP method, combined with the 6-311++G(d,p) level of DFT, provides more precise data when compared to alternative quantum chemical methods in the analysis of experimental data. Moreover, the CAM-B3LYP basis set was employed to theoretically examine electronic absorption spectra in the gas phase (TD-DFT) using polarized split-valence 6-311++G(d,p) basis sets. Additionally, the application of the Corrected Linear Response Polarizable Continuum Model (CLR

Table 1 Calculated E_{LUMO}, E_{HOMO}, energy band gap, ionization potential (*IP*), electron affinity (*EA*), electronegativity (χ), global hardness (η), chemical potential (v), global electrophilicity index (ω), global softness (*S*) and additional electronic charge (ΔN_{max}) in eV for the reactants **1** & **2** and the expected products **3** &**APPQ**, using B3LYP/6–311++G(d,p)

Parameters	1	2	3	APPQ	Ref. (Ans et al. 2022)	Ref. (Ans et al. 2019e)	Ref. (Siddique et al. 2020)	Ref. (Siddique et al. 2022)
E_{HOMO}	−6.8473	−5.6530	−6.8416	−6.1834	−6.0155	−6.1431	−5.5262	−5.7865
E_{LUMO}	−2.7442	−0.5434	−2.7257	−2.3367	−2.4018	−2.3574	−2.0231	−1.8006
Energy gap, (E_g)	4.1031	5.1095	4.1159	3.8466	3.6138	3.7857	3.5030	3.9859
Dipole moment, (μ)	10.6137	2.6572	7.7211	1.5580	8.6600	7.9700	1.9141	5.3085
I (eV)	6.8473	5.6530	6.8416	6.1834	6.0155	6.1431	5.5262	5.7865
A(eV)	2.7442	0.5434	2.7257	2.3367	2.4018	2.3574	2.0231	1.8006
χ(eV)	4.7957	3.0982	4.7836	4.2600	4.2085	4.2502	3.7746	3.7936
v(eV^{-1})	−4.7957	−3.0982	−4.7836	−4.2600	−4.2085	−4.2502	−3.7746	−3.7936
η(eV)	2.0516	2.5548	2.0579	1.9233	1.8069	1.8928	1.7516	1.9929
S(eV^{-1})	0.48702	0.391426	0.2430	0.513258	0.2767	0.2641	0.2855	0.2509
ω (eV)	5.6053	1.8786	5.5596	4.433508	4.9012	4.7717	4.0674	3.6105
ΔN_{max}	2.3375	1.2127	2.3245	2.133324	2.3291	2.2454	2.1549	1.9036
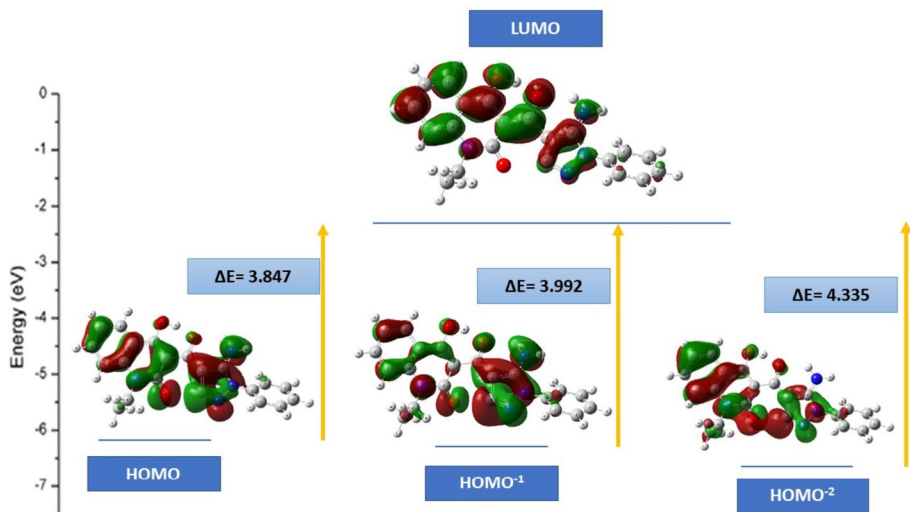
Fig. 2 Molecular orbitals (HOMO —»LUMO, HOMO^{-1} —»LUMO and HOMO^{-2} —» LUMO) of **APPQ** at the B3LYP/6-311G (d,p) basis set

PCM) in solvents like DMF, acetone, butanol, dioxane, toluene, and xylene demonstrates a strong agreement with the observed spectra, indicating practical utility. Without applying any symmetry restrictions, the primary structural characteristics of **APPQ**, such as bond lengths, bond angles, and dihedral angles, were optimized using the 6-311++G(d,p) basis set. Table 2 displays the corresponding values. Fig. 3 also shows the number of atoms in the compounds examined for this investigation.

Since there is no experimental data for **APPQ**, certain structural properties of **APPQ** have been compared to those of related systems with known crystal structures (Kafka et al. 2013; Vishnupriya et al. 2013). The experimental structure of a comparable molecule described in the literature and the optimized structure of **APPQ** were found to be remarkably comparable. The optimized structure of **APPQ** resembled the experimental structure of a related molecule from the literature, demonstrating the accuracy and realism of the optimization (Kafka et al. 2013; Vishnupriya et al. 2013). The chemical mentioned in the title has C1 symmetry. The bond lengths and angles of **APPQ** differed slightly from those noted in the literature (Kafka et al. 2013; Vishnupriya et al. 2013). The computations revealed that **APPQ** has a larger C–O bond length.

Particularly in the fingerprint area (1400–600 cm^{-1}) of the IR spectra of **APPQ**, there were numerous overlapping and complicated bands. In the current study, only distinct and clear-seen bands were discussed. The experimental and computed (scaled) wavenumbers are listed in Table 3 along with the assignments for each. To better match the experimental data, the computed wavenumbers were scaled down by 0.9613. The B3LYP-derived correlation coefficient (R2 = 0.996) revealed that the two sets of values were in good agreement with one another. The correlation graph in Fig. 3 lacks any dots between 1700 and 2850 cm^{-1} because the molecule's functional groups are not located there.
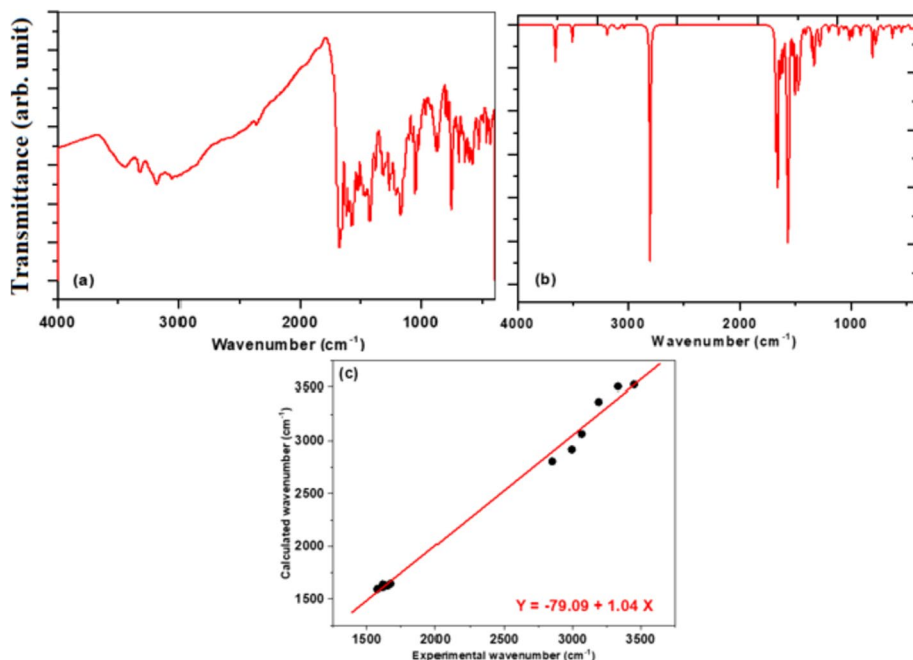
3.4 ^{1}H NMR and ^{13}C NMR spectroscopy of APPQ

The chemical shifts for ^{1}H and ^{13}C NMR were computed using the GIAO method. The chemical shifts for ^{1}H and ^{13}C NMR were computed using the GIAO method employing B3LYP and the 6-311 + +G(d,p) basis set. The experimental and calculated values of ^{1}H and ^{13}C NMR chemical shifts of the title compound are shown in Tables 4 and 5. The ^{1}H and ^{13}C NMR spectra charts are given in Figs. S1 and S2, respectively. Comparing the chemical shift data of ^{1}H and ^{13}C NMR appeared that, the symmetrical protons and carbons were observed as the signal value in the experimental chart but seen differently in the theoretical chart. For example, the methyl (CH_3) protons appeared in the experimental chart as a triplet signal at δ 1.21 ppm, but in the theoretical chart, three signals appeared at δ 1.08, 1.17, and 1.32 ppm. However, the value of the experimental signal between the three theoretical values indicates excellent agreement between the experimental and theoretical results. H-3$_{pyrazole}$ was seen theoretically at δ 7.49, while experimentally at δ 8.32. The amino protons were recorded theoretically as two signals at δ 4.34 and 7.67, meanwhile, these protons were seen experimentally as broad signals at δ 6.43. Further, the aromatic protons were seen theoretically in the range δ 7.46–7.87, while appeared experimentally in the range δ 6.71–8.23.

Further, some information was deduced from the data on chemical shifts of certain carbon atoms and their electron density. For example, the δ values for CH_2 and CH_3 carbons are 11.7/12.2 (cal./exp.) and 39.0/38.2 (cal./exp.), respectively, which corresponds to electron density −0.417/−0.100 (cal./exp.) confirming increasing of δ values for Sp3 hybridized carbons by decreasing the electron density (deshielding). In addition, the current compound contains two electrons repelling NH_2 and OH groups that increase the electron density over C-4$_{pyrazole}$ and C-3$_{quinoline}$, respectively. The electron density of C-4$_{pyrazole}$ (−0.131) is higher than C-3$_{quinoline}$ (1.463), this difference in electron density is directly related to the difference in electron negativity between nitrogen and oxygen atoms. Therefore, the δ value of C-4$_{pyrazole}$ (111.9/94.3; cal./exp.) is lower than C-3$_{quinoline}$ (115.8/111.5; cal./exp.), indicating more deshielding of C-4$_{pyrazole}$ as compared with C-3$_{quinoline}$. Moreover, although the pyrazole ring contains three carbon atoms, they differ in their chemical shift values due to the difference in electron density over these atoms. C-3$_{pyrazole}$ and C-5$_{pyrazole}$ are affected by the electron-withdrawing mesomeric of C=N$_{pyrazole}$, meanwhile, C-5$_{pyrazole}$ is additionally affected by the electron-withdrawing inductive effect of the NH_2 group. Thus, C-5$_{pyrazole}$ is more deshielded (electron density 0.696) than C-3$_{pyrazole}$ (electron density −0.014), and therefore, C-5$_{pyrazole}$ is observed at higher δ value (155.9/153.5; cal./exp.) than C-3$_{pyrazole}$ (146.1/140.6; cal./exp.). Because C-4$_{pyrazole}$ is only affected by electron repelling mesomeric effect of the NH_2 group, it has a higher electron density (0.131) inside the pyrazole ring and therefore lower δ value (111.9/94.3; cal./exp.). Finally, the chemical shift (δ) values of the two carbonyl carbons (C=O$_{quinoline}$ and C=O$_{ketone}$) are (163.8/171.8; cal./exp.) and (190.9/191.5; cal./exp.), respectively. These values agree well with the electron density over these carbons −1.44 and −0.74, respectively.

Figs. S1 and S2 depict the correlation graph between the computed and experimental chemical shifts for ^{1}H and ^{13}C NMR, respectively. The linear equation for the correlation graph is Y = 0.9 21 X + 0.448 for ^{1}H NMR and Y = 0.999 X—2.76 for ^{13}C NMR, where Y is the experimental chemical shift for ^{1}H and ^{13}C NMR and X is the computed ^{1}H and ^{13}C NMR chemical shift (in ppm.) (Al-Otaibi et al. 2015). The correlation coefficients (R2 = 0.96) for ^{1}H NMR and (R2 = 0.99) for ^{13}C NMR demonstrate that the

Table 2 (a) Selected optimized geometrical structure parameters for **APPQ** computed at B3LYP/6-311++G(d,p) and CAM/B3LYP/6-311++G(d,p)

Bond lengths (Å)	B3LYP/6-311++G(d,p)	CAM/B3LYP/6-311++G(d,p)	Exp. X-ray (Siddique et al. 2021b; Ibrahim et al. 2013)	Bond angles (°)	B3LYP/6-311++G(d,p)	CAM/B3LYP/6-311++G(d,p)	Exp. X-ray (Siddique et al. 2021b; Ibrahim et al. 2013)
C1-C6	1.361	1.385	1.374	<C8O18C9	107.38	111.22	108.89
C1=C2	1.384	1.452	1.409	<C5O23C7	124.36	123.52	124.24
C9-O18	1.367	1.374	1.355	<C8C25O28	116.71	121.12	118.98
C7-O23	1.482	1.445	1.355	<C1C7C8	107.78	109.56	112.54
C25=O28	1.230	1.251	1.248	<C1C6C5	119.25	121.21	121.91
C11-N10	1.347	1.368	1.363	<C4N10C11	117.32	118.45	118.23
N29-N30	1.381	1.392	1.431	<N32C31N30	113.58	125.46	120.64
N32-H34	1.036	1.037	1.017	<C27N29N30	107.71	106.94	109.57
O23-H24	0.982	0.985	0.989	<C31N32H33	120.26	125.48	126.39
C1-H20	1.067	1.073	0.98	<C7O23H24	107.38	110.11	111.96

Dihedral angles (°)	B3LYP/6-311++G(d,p)	CAM/B3LYP/6-311++G(d,p)
<O18C9C8C7	68.927	90.765
<O23C7C8C25	7.710	8.852
<C26C31N32H33	175.58	179.92
<N32C31N30C36	−180.14	−179.97
<N30C31N32H34	0.251	0.723
<H20C1C6H21	−0.055	−0.382
<C6C1C7C8	179.83	179.97

Fig. 3 **a** Experimental and **b** Calculated IR spectrum, **c** Correlation graph between experimental and calculated IR wavenumbers of **APPQ** at B3LYP/6-311 + +G (d,p)

theoretical and experimental chemical shifts agree well. Except for the proton of the OH group, which is not seen in the spectrum, the observed and computed chemical shift values in ^{1}H NMR exhibit good agreement (Szafran et al. 2007).

3.5 UV–Visible absorption spectroscopy

The UV–Vis absorption spectrum was theoretically computed using the TD-DFT method, the 6-311 + +G(d,p) basis set, the CAM-B3LYP functional, and the solvent

Table 3 Experimental and calculated vibrational frequencies in cm^{-1} of **APPQ** using DFT/B3LYP 6-311 + +G (d, p) with the proposed assignments

No	IR stretching vibrational bands		Stretching vibrational assignments	References
	Exp	Calculated (B3LYP)		
1	3450	3525	O–H	Liu et al. (2012)
2	3332, 3190	3369, 3507	NH_2	Liu et al. (2012)
3	3066	3066	C–H$_{aromatic}$	Liu et al. (2012)
4	2994, 2850	2919, 2806	C–H$_{aliphatic}$	Liu et al. (2012)
5	1675	1647	C=O$_{ketone}$	Govindarajan et al. (2012)
6	1655	1630	C=O$_{quinolone}$	Govindarajan et al. (2012)
7	1618	1613	C=N	Govindarajan et al. (2012)
8	1578	1595	C=C	Govindarajan et al. (2012)

Table 4 Experimental and calculated ^{1}H NMR chemical shift values for **APPQ** using B3LYP/6-311 + +G (d,p)

^{1}HNMR chemical shift values				
Hydrogen numbering as in Fig. 1	Type of hydrogen atom	Calculated chemical shift (δ, ppm)	Experimental chemical shift (δ, ppm)	Electron density
16	CH$_3$	1.0852	1.21	0.14
15		1.1561		0.194
17		1.3244		0.133
13	CH$_2$	3.6534	4.27	0.199
14		4.8437		0.149
33	NH$_2$	4.3487	6.43	0.272
34		7.6632		0.336
24	OH	5.7875	OH, not observed	0.445
20	Ar–H	7.4631	6.71	0.160
46	H-3$_{pyrazole}$	7.4986	8.32	0.244
43	Ar–H	7.5021	6.9	0.156
22	Ar–H	7.5288	7.2	0.145
21	Ar–H	7.6752	7.43	0.199
44	Ar–H	7.6982	7.55	0.189
42	Ar–H	7.7065	7.56	0.185
45	Ar–H	7.8341	7.61	0.207
41	Ar–H	7.857	7.79	0.207
19	Ar–H	7.8737	8.23	0.182

effect was considered using the Integral Equation Formalism Polarizable Continuum Model (IEFPCM) (Karabacak 2009; Roeges et al. 1994). The utilization of the CAM-B3LYP method, coupled with the 6-311 + +G(d,p) level of DFT, yields more precise data compared to alternative quantum chemical approaches when cross-referenced with experimental data. Additionally, the CAM-B3LYP method, employing the Coulomb-attenuating method and the polarized split-valence 6-311 + +G(d,p) basis sets, is employed to theoretically investigate electronic absorption spectra in the gas phase (TD-DFT). Furthermore, the inclusion of the CLR-PCM in diverse solvents such as DMF, acetone, butanol, dioxane, toluene, and xylene demonstrates a commendable.

In Table 6, the vertical excitation energies, oscillator strength (*f*), and associated absorption wavelengths of the experimental and manufactured UV data are compared. The TD-DFT results for the low-intensity bands (Q-region) and high-intensity bands were obtained in the gas phase as well as in polar solvents (butanol, DMF, and acetone) and non-polar solvents (dioxane, toluene, and xylene) to understand the effect of polarity on electronic transitions between HOMO and LUMO energy levels of **APPQ** (Karabacak 2009; Roeges et al. 1994). The corresponding spectra are shown in Fig. 4 along with the electronic spectra of **APPQ** in butanol, DMF, and acetone. Dioxane, toluene, and xylene can be used to create a spectrum with seven bands at 460, 430, 385, 365, 295, 280, and 265 nm. There were slight shifts in the band locations as the solvent polarity increased from dioxane, toluene, and xylene to butanol, DMF, and acetone. This implies independence from the solvent because the polarity of both the

Table 5 Experimental and calculated ^{13}C NMR chemical shift values for **APPQ** using B3LYP/6-311+ +G (d,p)

^{13}CNMR Chemical shift values

Carbon Numbering as in Fig. 1	Type of carbon atom	Calculated ^{13}C NMR (ppm)	Experimental ^{13}C NMR (ppm)	Electron density
12	CH$_3$	11.7438	12.2	−0.417
11	CH$_2$	39.0759	38.2	−0.100
26	C-4 pyrazole	111.9232	94.3	−0.131
8	C-3 quinoline	115.7912	111.5	1.465
5	C-4a quinoline	116.8755	118.1	0.428
3	Ar–C	117.7273	120.5	−0.332
35	Ar–C	122.784	121.2	0.205
6	Ar–C	123.8196	123.6	−0.525
1	Ar–C	124.5338	126.4	−0.598
38	Ar–C	126.8934	121.2	0.100
40	Ar–C	130.5273	127.0	−0.405
37	Ar–C	133.0232	128.2	−0.013
39	Ar–C	133.9968	128.2	−0.178
2	Ar–C	136.8199	129.5	−0.248
36	Ar–C	144.1886	135.3	−0.721
4	C-8a quinoline	144.9416	139.0	0.096
27	C-3 pyrazole	146.0675	140.6	−0.014
31	C-5 pyrazole	155.9847	153.5	0.696
7	C-4 quinoline	162.2802	161.3	−0.05
9	C=O quinoline	163.8446	171.8	−1.444
25	C=O ketone	190.9694	191.5	−0.741

excited and ground states is consistent across many solvents. Butanol, DMF, and acetone resulted in a decrease in the intensity of the band. As shown by their intensities, which range from −1000 to 11,000, all seven bands were thought to be the result of transitions involving the $(\pi-\pi^*)$ and $(n-\pi^*)$ states.

The ten highest-occupied molecular orbitals $(\varphi_{59}-^1\varphi_{90})$ and the ten lowest-occupied molecular orbitals $(\varphi_{71}-^1\varphi_{80})$ are involved in electron excitation for the excited configurations in the **APPQ** model. The calculated transitions and transitions observed in the experiments match each other satisfactorily. The first $(n-\pi^*)^1$ state is centered at approximately 450, 430, and 450 nm in dioxane, toluene, and xylene, respectively, which are non-polar solvents. With wavelengths of approximately 460, 450, and 460 nm, the theoretical predictions for this band are in excellent agreement with the experimental observations. $\varphi_{60-70}-1\varphi_{71-85}$ are the configurations in charge of this band. A wavelength of 450 nm was obtained from the calculations in the gas phase.

At approximately 440, 439, and 440 nm, the same $(n-\pi^*)1$ state was observed in polar solvents (butanol, DMF, and acetone). According to Table 6, the theoretical calculations in these solvents successfully recreated the bands at approximately 445, 447, and 450 nm. The second through seventh states exhibit a similar pattern, which is consistent with the first state. The $n-\pi^*$ and $\pi-\pi^*$ transitions were typified by these

apparent absorption bands. The solvent causes a 3–4 nm blue or red shift in the absorption band, which corresponds to the maximal absorption of **APPQ**. The theoretical and experimental vertical excitation energies and related oscillator strengths for **APPQ** are listed in Table 6.

3.6 Molecular electrostatic potential

The electrophilic (electron-rich region) and nucleophilic (electron-poor region) reactive sites can be estimated using the molecular electrostatic potential (MESP). In the MESP, the red and blue areas represent electron-rich and electron-poor regions, respectively, whereas the green zone represents a virtually neutral region. The change in electrostatic potential created by a molecule is substantially responsible for the binding of a drug to its receptor-binding sites since the binding site in general is predicted to comprise opposite areas of electrostatic potential. An MESP map of the **APPQ** is displayed in Fig. 5 and was created using the Gauss View software with optimized geometry. Assessment of electrophilic (electron-rich) and nucleophilic (electron-poor) reactive sites is possible using the molecular electrostatic potential (MESP). In the MESP, the green zone denotes a roughly neutral region, whereas the red and blue portions denote the electron-rich and electron-poor regions, respectively. The change in electrostatic potential brought on by a chemical plays a key role in the binding of a drug to its receptor-binding sites because binding sites often contain areas of opposite electrostatic potential. An MESP map of the **APPQ** is shown in Fig. 5 and was produced using the Gauss view program at its optimized geometry. The MESP of the molecule, which is distinguished by the yellowish-red color, makes it easy to see the most significant negative potential region surrounding the oxygen and nitrogen atoms of the (nitrile group), as well as the binding site for electrophilic assault. The most positively charged protons in the molecule are protons H24, H33, and H34, whereas the rest of the molecule appears to have a neutral electrostatic potential.

3.7 Natural bond orbital analysis

B3LYP/6-311 + +G(d,p) and Gaussian09 software were used to calculate the Natural Bond Orbital (NBO). Charge transfer, conjugative interactions, intramolecular bonding, and intermolecular bonding may all be investigated using these computations. The stabilizing energy value depends on the degree of coupling between the electron donors and acceptors, as well as the degree of conjugation in the system. The second-order Fock matrix was used in the NBO analysis to examine how the donor (i) and acceptor (j) bonds interact. Through this interaction, an empty non-Lewis orbital acquires the electron occupancy that was previously in the idealized Lewis structure. The delocalization from donor (i) to acceptor (j) stabilizes at a certain energy E(2). In this system, a larger E(2) value denotes more conjugation and stronger interaction between the electron donors and acceptors. The intense interactions discovered using NBO analysis are shown in Table 7. System stabilization is caused by strong intramolecular hyperconjugative interactions, which increase electron density (ED) and intramolecular charge transfer (ICT). the following are some particular interactions:

Natural Bond Orbital (NBO) calculations (Cheng et al. 1991) were carried out using the B3LYP/6-311 + +G(d,p) method in the Gaussian09 program. This offers a helpful starting point for research on intramolecular and intermolecular bonding and bond interactions,

Table 6 Experimental and Computed excitation energies (eV), electronic transition configurations, and oscillator strengths (f) for the optical transitions of the absorption bands in the UV–vis. regions (involving HOMOs) of **APPQ** at CAM-B3LYP/6-311 + + G(d,p)

Medium	Transition	Excitation energies	Type of transition	λ_{max}/nm Th and Ex	Oscillator strengths (f)	Configuration composition corresponding transition orbital
Gas phase	S0→S1	3.51	n-π*	450	0.1079	0.24 (64→70); 0.30 (66→68); −0.23 (66→69); −0.14 (66→71); 0.26 (67→68); −0.30 (67→69)
	S0→S2	4.02	n-π*	415	0.3016	0.18 (60→71); 0.20 (61→75); −0.13 (66→68); −0.16 (65→71); 0.27 (66→69); −0.36 (67→69)
	S0→S3	4.75	π-π*	380	0.6002	0.37 (62→73); 0.45 (64→68); 0.34 (64→69)
	S0→S4	3.98	π-π*	350	0.2409	−0.43 (60→69); −0.25 (60→69); −0.23 (66→69)
	S0→S5	5.35	π-π*	295	0.4429	0.12 (60→70); 0.10 (61→69); −0.12 (62→71); −0.25 (65→72); 0.17 (63→73); −0.33 (63→78)
	S0→S6	5.55	π-π*	285	0.7281	0.20 (59→68); 0.12 (61→69); −0.15 (66→71); −0.23 (67→69); 0.15 (66→71); 0.11 (61→72)
	S0→S7	6.83	π-π*	265	0.3280	0.10 (63→78); 0.52 (61→70); −0.15 (64→71); −0.28 (66→72); 0.12(66→68); −0.31 (67→69)
Acetone	S0→S1	3.48	n-π*	450 440	0.1053	0.23 (65→73); 0.21 (66→68); −0.33 (66→69); −0.11 (64→71); 0.16 (67→72); −0.30 (67→69)
	S0→S2	4.12	n-π*	410 400	0.3096	0.24 (63→74); 0.11 (66→69); −0.13 (66→70); −0.35 (66→72); 0.27 (66→69); −0.36 (67→71)
	S0→S3	2.97	π-π*	375 350	0.3715	0.15 (61→70); 0.52 (64→68); 0.34 (65→69)
	S0→S4	3.98	π-π*	340 320	0.6065	−0.26 (63→69); −0.20 (66→71); 0.11 (67→72); −0.13 (66→74); 0.27 (66→71)
	S0→S5	5.10	π-π*	295 285	0.5628	0.22 (63→68); 0.10 (66→69); −0.12(67→71); −0.35 (66→72); 0.27 (63→73); −0.33 (67→78)
	S0→S6	5.24	π-π*	280 265	0.4167	0.20 (65→70); 0.12 (63→69); −0.15 (60→71); −0.23 (67→80); 0.15 (66→81); 0.11 (67→72)
	S0→S7	6.75	π-π*	250 215	0.5005	0.15 (59→68); 0.52 (61→70); −0.15 (64→71); −0.28 (66→72); 0.12(66→68); −0.31 (67→69)

Table 6 (continued)

Medium	Transition	Excitation energies	Type of transition	λ_{max}/nm Th and Ex	Oscillator strengths (f)	Configuration composition corresponding transition orbital
Dioxane	S0−>S1	3.51	n–π*	460 / 450	0.1089	0.22 (65−>75); 0.32 (66−>68); −0.23 (66−>69); −0.14 (67−>81); 0.26 (67−>68); −0.30 (67−>69)
	S0−>S2	4.00	n–π*	430 / 420	0.4046	−0.18 (60−>78); 0.22 (61−>69); −0.13 (66−>68); −0.25 (66−>80); 0.27 (66−>69); −0.36 (67−>69)
	S0−>S3	2.98	π–π*	385 / 366	0.5012	0.11 (60−>70); 0.45 (63−>68); 0.24 (64−>69);0.15(65−>71)
	S0−>S4	4.09	π–π*	365 / 335	0.5719	−0.23 (60−>68); −0.25 (62−>69); 0.51 (64−>70);−0.33 (66−>68); −0.25 (66−>69)
	S0−>S5	5.23	π–π*	295 / 290	0.4471	0.21 (62−>68); 0.10 (63−>69); −0.12 (66−>71); −0.35 (66−>72); 0.17 (66−>73); −0.33 (66−>78)
	S0−>S6	5.46	π–π*	280 / 270	0.5550	0.34 (60−>68); 0.10 (61−>70); −0.53 (64−>71); −0.28 (66−>72); 0.22(66−>69); −0.31 (67−>72)
	S0−>S7	6.14	π–π*	265 / 255	0.2139	0.20 (58−>68); 0.52 (60−>70); −0.15 (64−>71); −0.28 (63−>72); 0.12(65−>69); −0.31 (67−>82)

Table 6 (continued)

Medium	Transition	Excitation energies	Type of transition	λ_{max}/nm Th and Ex	Oscillator strengths (f)	Configuration composition corresponding transition orbital
Butanol	S0→S1	3.42	n–π*	445 440	0.1052	–0.24 (63→69); 0.21 (66→69); –0.33 (66→70); –0.31 (66→71); 0.41(67→72); –0.13 (67→69)
	S0→S2	3.89	n–π*	415 410	0.3096	0.11 (66→71); 0.21 (66→69); –0.13 (66→70); –0.25 (66→72); 0.27 (66→74); –0.36 (67→71)
	S0→S3	4.03	π–π*	375 355	0.4536	0.20 (59→70); 0.25 (61→68); 0.34 (65→69) 0.34 (64→71); 0.21 (66→69); –0.13 (67→70)
	S0→S4	4.38	π–π*	340 325	0.6273	–0.26 (63→69); –0.20 (66→71); 0.11 (67→72); –0.33 (66→74); 0.27 (66→71)
	S0→S5	5.20	π–π*	298 285	0.5616	0.12 (63→68); 0.10 (66→69); –0.12 (67→71); –0.25 (66→72); 0.27 (63→73); –0.33 (67→78);
	S0→S6	5.24	π–π*	280 250	0.4084	0.10 (60→68); 0.12 (63→69); –0.15 (60→71); –0.33 (67→70); 0.15 (66→81); 0.11 (67→72)
	S0→S7	5.88	π–π*	265 230	0.6012	0.11 (59→68); 0.52 (61→70); –0.15 (64→71); –0.18 (66→72); 0.12(66→68); –0.31 (67→69)

Table 6 (continued)

Medium	Transition	Excitation energies	Type of transition	λ_{max}/nm Th and Ex	Oscillator strengths (f)	Configuration composition corresponding transition orbital
DMF	S0–>S1	2.89	n–π*	447 439	0.1153	0.23 (61–>70); 0.21 (66–>68); –0.33 (66–>69); –0.18 (66–>71); 0.16 (67–>72); –0.30 (67–>69)
	S0–>S2	3.52	n–π*	421 400	0.3396	0.34 (66–>71); 0.11 (66–>69); –0.13 (66–>70); –0.15 (66–>72); 0.27 (66–>69); –0.36 (67–>71)
	S0–>S3	4.06	π–π*	370 350	0.4735	0.25 (61–>70); 0.52 (64–>68); 0.34 (65–>69)
	S0–>S4	4.87	π–π*	330 312	0.5365	–0.26 (63–>69); –0.20 (66–>71); 0.11 (67–>72); –0.33 (66–>74); 0.27 (66–>71)
	S0–>S5	5.25	π–π*	295 280	0.3628	0.32 (63–>68); 0.10 (66–>69); –0.12 (67–>71); –0.15 (66–>72); 0.27 (63–>73); –0.33 (67–>78)
	S0–>S6	5.90	π–π*	281 255	0.4067	0.20 (60–>68); 0.12 (63–>69); –0.15 (60–>71); –0.33 (67–>70); 0.15 (66–>81); 0.11 (67–>72)
	S0–>S7	6.05	π–π*	260 220	0.6005	0.11 (59–>68); 0.52 (61–>70); –0.15 (64–>71); –0.28 (66–>72); 0.12(66–>68); –0.31 (67–>69)

Table 6 (continued)

Medium	Transition	Excitation energies	Type of transition	λ_{max}/nm Th and Ex	Oscillator strengths (f)	Configuration composition corresponding transition orbital
Toluene	S0->S1	3.81	n–π*	450 430	0.1087	0.22 (62–>72); 0.20 (66–>68); –0.23 (66–>69); –0.34 (66–>71); 0.26 (67–>68); –0.30 (67–>69)
	S0->S2	4.00	n–π*	425 405	0.2345	–0.31 (59–>71); 0.22 (61–>69); –0.13 (66–>68); –0.15 (66–>71); 0.27 (66–>69); –0.36 (67–>69);
	S0->S3	4.31	π–π*	380 350	0.3420	0.11 (60–>70); 0.45 (63–>68); 0.24 (64–>69);0.15(65–>71)
	S0->S4	3.79	π–π*	310 300	0.4853	–0.34 (60–>68); –0.38 (62–>69); 0.51 (64–>70);–0.33 (66–>68); –0.25 (66–>69)
	S0->S5	5.22	π–π*	285 265	0.5330	0.11 (62–>68); 0.10 (63–>69); –0.12 (66–>71); –0.25 (66–>72); 0.17 (66–>73); –0.33 (66–>78)
	S0->S6	5.64	π–π*	277 256	0.6354	0.34 (60–>68); 0.10 (61–>70); –0.53 (64–>71); –0.18 (66–>72); 0.22(66–>69); –0.31 (67–>72)
	S0->S7	6.04	π–π*	240 220	0.2015	0.11 (60–>68); 0.52 (61–>70); –0.15 (64–>71); –0.18 (63–>72); 0.12(65–>69); –0.31 (67–>82)

Table 6 (continued)

Medium	Transition	Excitation energies	Type of transition	λ_{max}/nm Th and Ex	Oscillator strengths (f)	Configuration composition corresponding transition orbital
Xylene	S0–>S1	3.51	n–π*	460 450	0.1089	0.22 (65–>75); 0.32 (66–>68); –0.23 (66–>69); –0.14 (67–>81); 0.26 (67–>68); –0.30 (67–>69)
	S0–>S2	4.00	n–π*	430 420	0.4046	–0.18 (60–>78); 0.22 (61–>69); –0.13 (66–>68); –0.25 (66–>80); 0.27 (66–>69); –0.36 (67–>69)
	S0–>S3	2.98	π–π*	385 366	0.5012	0.11 (60–>70); 0.45 (63–>68); 0.24 (64–>69);0.15(65–>71)
	S0–>S4	4.09	π–π*	365 335	0.5719	–0.23 (60–>68); –0.25 (62–>69); 0.51 (64–>70);–0.33 (66–>68); –0.25 (66–>69)
	S0–>S5	5.23	π–π*	295 290	0.4471	0.21 (62–>68); 0.10 (63–>69); –0.12 (66–>71); –0.35 (66–>72); 0.17 (66–>73); –0.33 (66–>78)
	S0–>S6	5.46	π–π*	280 270	0.5550	0.34 (60–>68); 0.10 (61–>70); –0.53 (64–>71); –0.28 (66–>72); 0.22(66–>69); –0.31 (67–>72)
	S0–>S7	6.14	π–π*	265 255	0.2139	0.20 (58–>68); 0.52 (60–>70); –0.15 (64–>71); –0.28 (63–>72); 0.12(65–>69); –0.31 (67–>82)

as well as charge transfer and conjugative interactions in molecular systems. The higher the stabilizing energy value, the stronger the bond between electron donors and electron acceptors, or, more specifically, the greater the tendency of electron donors to donate to electron acceptors, and the greater the degree of conjugation of the entire system. The donor (i)–acceptor (j), or the interaction between the donor and acceptor level bonds, was examined in the NBO investigation using the second-order Fock matrix (Karabacak 2009; Roeges et al. 1994).

This interaction causes the vacant non-Lewis orbital to lose its occupancy due to the electron NBO concentration of the idealized Lewis structure. Table 7 illustrates the potential for intense engagement in NBO. The system was stabilized as a result of increased electron density (ED) and intramolecular charge transfer (ICT) due to strong intramolecular hyperconjugative interactions. 24.86 kcal mol^{-1} is stabilised between C3–C4 from N32 of n1 (N32) * (C3–C4), which raises ED (0.45e).

3.8 Natural population analysis and natural charges

Table 8 displays the natural charge and population of the total electrons on the subshells, as well as the natural electronic configuration of the **APPQ** active sites at the B3LYP/6-311 + +G (d,p) level. The most negative centers were found in O18, O23, O28, N10, N29, N30, and N32. The most positive centers were found in the protons (H24, H33, and H34) and carbon atoms connected to these heteroatoms, indicating a restricted supply of electrons from the static electricity of the **APPQ** molecule. In addition, according to a natural population study, **APPQ** has 98 coordinated electrons in the subshells, 98 total Lewis electrons, and 98 non-Lewis electrons.

3.9 Nonlinear optical analysis

In this investigation, the initial hyperpolarizability of the title compound was determined using the finite field method and B3LYP and CAM-B3LYP/6-311 + +G (d, p) basis sets (Zhang et al. 2010). Table 9 displays the results for the electronic dipole moment μ_i (i = x, y, z), polarizability α_{ij}, and first-order hyperpolarizability βijk. The calculated dipole moment for the B3LYP level was 1.5580 D, whereas that for the CAM-B3LYP level was 1.5370 D. A well-known molecule called P Nitroaniline (PNA) is utilized as a model system to investigate the nonlinear optical (NLO) characteristics of molecular systems. Because the title chemical had no experimental values listed in the literature, PNA was used in this investigation as a reference molecule. A B3LYP level's computed polarizability α_{tot}, of 52.14×10^{-24} esu and the calculated polarizability of the CAM-B3LYP level of 46.89×10^{-24} esu are both twice as high as the polarizability of the PNA molecule.

The new compound has a computed first hyperpolarizability total of 35.52×10^{-33} esu for B3LYP level and 15.82×10^{-33} esu for CAM-B3LYP level, which is greater (by two times for B3LYP level and CAM-B3LYP level) than that of the typical NLO material PNA (15.5×10^{-33} esu) (Cheng et al. 1991). Furthermore, **APPQ's** second-order hyperpolarizability, or y, was calculated to be 4.82×10^{-35} esu for B3LYP levels and -2.04×10^{-35} esu for CAM-B3LYP levels, which is three times higher than that of PNA molecules. Additionally, for the molecule under investigation, the lowest value of DR and the greatest value of HRS both confirmed short bond lengths, indicating improved selectivity. We conclude that
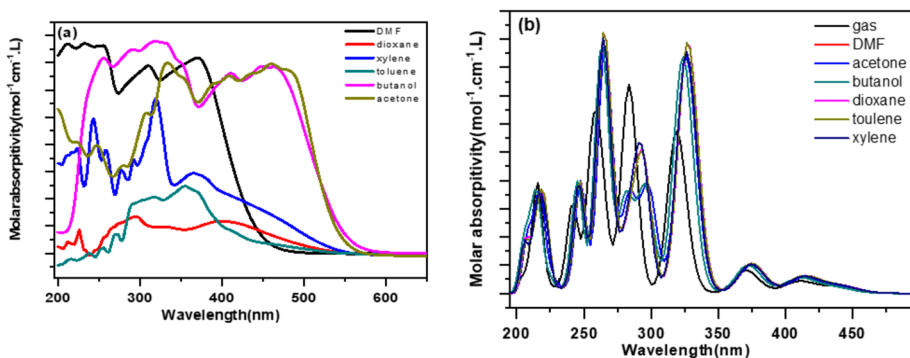
Fig. 4 Experimental and calculated electronic absorption spectra of **APPQ** in different solvents

the current compound is a desirable subject for future investigations of nonlinear optical characteristics.

3.10 Thermodynamic properties

The values of some thermodynamic parameters for the current compound, including zero-point vibrational energy, rotational temperatures, rotational constants, and energies at a standard temperature of 298 K, were obtained at the HF and DFT levels using the B3LYP/CAM-B3LYP functional with the $6\text{-}311++G(d,p)$ basis set (Table 10). The total energy and translational, rotational, and vibrational values are somewhat higher when calculated in HF than in B3LYP or CAM-B3LYP. They can be used to predict chemical reaction trajectories in the thermochemical field and to determine other thermodynamic energies using thermodynamic function relationships and the second law of thermodynamics (Zhang et al. 2010). It was impossible to apply any of the thermodynamic calculations to a solution because they were performed in the gas phase.

(a) Total density   (b) ESP   (c) MEP
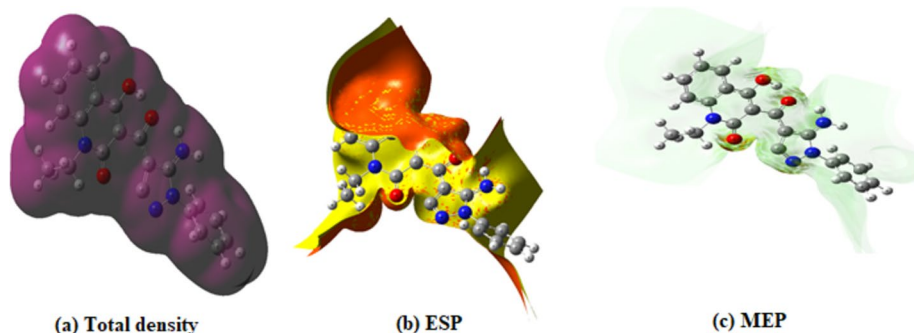
Fig.5 Molecular surfaces **a–c** of **APPQ** using $B3LYP/6\text{--}311++G(d,p)$

3.11 Morphological characterization of APPQ

Scanning electron microscopy (SEM) is a highly effective technique that allows high-resolution analysis of the morphology of diverse materials. SEM offers useful insights into the structure and surface characteristics of these materials when analyzing their aggregation and microrod forms. Figures 6a–d show the SEM images of the surface morphology of **APPQ** at various magnifications. The photos show that the surface of **APPQ** is composed of tightly packed, agglomerated micro rods that have a wide variety of shapes. Furthermore, the dispersion of micro rods is not uniform, even if the surface retains a homogeneous structure. Each aggregate is made up of numerous distinct micro-rods with an average size ranging from 1 to 3 μm, according to an analysis of the morphological microstructural characteristics.

These micro rods can be imaged in depth using scanning electron microscopy (SEM), which enables researchers to examine their sizes, surface textures, and other important properties. Studying their growth processes, characteristics, and possible uses requires such information. The **APPQ** sizes that were discovered provide proof of the superior calibration of the deposited **APPQ** surface. This superior quality is anticipated to enable effective charge carrier transmission, leading to exceptional electrical and optoelectronic performances (El-Mahalawy et al. 2022).

3.12 Photoluminescence properties of APPQ

The photoluminescence (PL) spectrum of **APPQ** at ambient temperature is shown in Fig. 7. The spectrum was obtained at an excitation wavelength of 350 nm. With an energy of 2.17 eV, the direct transition of **APPQ** through the inter-band is responsible for the observed band in the spectrum. The impact of the molecular vibrational dynamics on the emission spectra is revealed by the Lorentz vibronic subbands. In particular, there were broad peaks with three vibronic sub-bands centered at 570 nm. These sub-bands have peaks at 450 and 560 nm and a lower peak at 660 nm.

According to previous studies, the singlet–singlet state transition (S2–S0, S1–S0) is responsible for the emission peaks in the visible region. The molecule travels from a higher-energy excited state (S2 or S1) to a lower-energy ground state (S0) during transitions that involve electronic energy levels. The resulting energy differential correlates with the emitted visible light and creates visible peaks in the spectrum (Almotiri et al. 2022).

3.13 Optical characteristics of APPQ thin films

The correlation between the photon energy and absorption coefficient is shown in Fig. 8a. A visible Q-band at 2.9 eV (427.6 nm) and a UV Soret band at 3.25 eV (381.53 nm) are two different bands with significant absorption peaks. According to Yousef et al. (2012), these peaks are a result of electronic transitions between the molecular orbitals $\pi \rightarrow \pi^*$ and $n \rightarrow \pi^*$. The remarkable absorption properties of **APPQ** thin films offer important benefits for a variety of photodetection applications and high-efficiency photovoltaic cells (Roushdy et al. 2022).

Figure 7b shows that the skin depth ($= 1/\alpha$) significantly decreased with increasing photon energy in the absorption spectral area (Hassanien et al. 2016). This decline is explained by the fact that some of the incident photon energy is used to create electron–hole pairs. It should be noted that the skin depth was greater than the film thickness (350 nm) by approximately 2200 nm. This implies that regardless of the incident photon energy within the absorption range of the film, the full bulk of the sample can be effectively used for

Table 7 Second order perturbation theory analysis of Fock matrix in NBO basis $E^{(2)}$ values (kcal/mol) for the optimized structure **APPQ**

Donor	Type	ED(i)(e)	Acceptor	Type	ED(i)(e)	$E^{(2)a}$(kcal/mol)	E(j)-E(i)^b(a.u)	F(ij)^c(a.u)
BD C1-C2	π	1.7602	BD*C3-C4	π*	0.4517	24.86	0.28	0.076
BD C1-C2	π	1.7652	BD*C5-C6	π*	0.3546	19.92	0.29	0.066
BD C3-C4	π	1.7721	BD*C8-C7	π*	0.3654	23.70	0.30	0.072
BD C5-C6	π	1.7854	BD*C1-C2	π*	0.2617	21.90	0.32	0.071
BD C8-C7	π	1.7523	BD*C23-C25	π*	0.2463	25.34	0.33	0.077
BDC23-C25	π	1.7860	BD* C8-C7	π*	0.3654	15.78	0.30	0.055
BD C4-C5	σ	1.9826	BD*C6-C26	σ*	0.0421	7.21	0.85	0.058
BDC16-C22	π	1.7290	BD*C5-C16	π*	0.4104	27.49	0.31	0.079
BDC5-C16	π	1.7936	BD*C27-N37	π*	0.1219	22.89	0.45	0.087
LP(2) O18		1.7645	BD*C3- C4	π*	0.4517	35.76	0.36	0.099
LP(2) O23		1.7645	BD*C17-O12	π*	0.2756	37.85	0.38	0.098
LP(2) O28		1.8521	BD*C22-C23	σ*	0.0769	19.92	0.71	0.103
LP(1) N10		1.5970	BD* C8- C7	π*	0.3654	53.93	0.32	0.114
LP(1) N29		1.5970	BD*C5-C16	π*	0.4104	48.62	0.34	0.106
LP(1) N30		1.9778	RY*C28	σ*	0.0267	17.90	1.36	0.132
LP(1) N32		1.9771	BD*C26-C27	σ*	0.0438	15.59	1.21	0.102
BD*C3-C4	π*	0.4517	BD*C1-C2	π*	0.3718	145.07	0.04	0.085
BD*C5-C6	π*	0.3546	BD*C1-C2	π*	0.3718	185.38	0.01	0.082
BD*C8-C7	π*	0.3654	BD*C4-O15	π*	0.2756	155.50	0.01	0.076
BD*C16C22	π*	0.3654	BD*C23-C25	π*	0.2463	176.55	0.01	0.078
BD*C5-C16	π*	0.4104	BD*C23-C25	π*	0.2463	195.23	0.01	0.077

[a] $E^{(2)}$ means energy of hyper conjugative interactions (stabilization energy)

[b] Energy difference between donor and acceptor i and j NBO orbitals

[c]$F_{(i, j)}$ is the Fock matrix element between i and j NBO orbital

$LP_{(n)}$ is a valence lone pair orbital (n) on atom

the creation of electron–hole pairs. The suitability of the **APPQ** film as an active layer in organic photovoltaic devices was demonstrated by the correlation between its high skin depth values and comparatively low extinction coefficient values.

To determine the type of electronic transition and energy gap (E_g) value, Tauc's relation was employed (Tauc et al. 1972). Figure 8c illustrates the link between the photon energy and $(E)^{1/2}$, which results in an indirect energy gap of approximately 2.35 eV. This figure is less than the energy gap discovered by calculating the HOMO–LUMO energy difference by DFT analysis, as previously reported. Because the DFT method relies on approximations and exchange–correlation functionals, the energy gap for organic compounds derived from calculations is greater than that from experimental measurements. The complicated nature of the electronic correlations and excitations in organic compounds may not be

Table 8 Natural charge, natural population analysis for **APPQ**

Atom No	Natural Charge	Natural Population				Natural electronic Configuration
		Core	Valence	Rydberg	Total	
O18	−0.33029	0.999	3.32379	0.00662	4.3303	[core]2S(0.85)2p(2.47)
O23	−0.32976	0.999	3.32339	0.00651	4.3298	[core]2S(0.82)2p(2.50)
O28	−0.35621	0.999	3.34982	0.00652	4.3562	[core]2S(0.85)2p(2.50)
N10	−0.23177	0.999	2.72140	0.01076	3.7318	[core]2S(0.60)2p(2.12)
N29	−0.17363	0.999	2.66180	0.01212	3.6736	[core]2S(0.74)2p(1.92)4p(0.01)
N30	−0.17747	0.999	2.66185	0.01604	3.6775	[core]2S(0.60)2p(2.06)4p(0.01)
N32	−0.38768	0.999	2.88065	0.00735	3.8877	[core]2S(0.66)2p(2.22)
H24	0.25300	0.000	0.24330	0.00370	0.2470	1S(0.24)
H33	0.19531	0.000	0.30328	0.00141	0.3047	1S(0.30)
H34	0.21655	0.000	0.28178	0.00167	0.2834	1S(0.28)
	Core	27.98819 (99.958% of 28)				
	Valence lewis	67.14430 (95.920% of 70)				
	Total lewis	95.13249 (97.074% of 98)				
	Valence non-lewis	2.65239 (2.707% of 98)				
	Rydberg non-lewis	0.21512 (0.220% of 98)				
	Total non-lewis	2.86751 (2.926% of 98)				

accurately captured by these approximations, causing variations in the expected energy gap (Abdul Mumit et al. 2020).

The Urbach empirical law connects the absorption coefficient (α) to the photon energy (h v) for low-energy photons (shown in Fig. 8d) (Urbach et al. 1953). In general, it is believed that this energy is caused by localized states that arise within the optical gap. These states in amorphous and low-crystalline materials are connected to the disorder. The large absorption band within the optical gap in the case of **APPQ** indicated an Urbach energy of approximately 250 meV.

3.14 Current–voltage and photovoltaic characteristics of APPQ-based heterojunction

A schematic diagram of the **APPQ** /n-Si heterojunction is shown in Fig.9 for measuring the dark current density–voltage (*J–V*) under the influence of light. The charge transport mechanism in the heterojunction based on **APPQ** was investigated using current–voltage measurements at a temperature of 300 K, shown in Fig. 10a. The measured current–voltage (*J–V*) characteristics show how diodes behave in both forward and reverse biases. At lower voltages, the current initially remained constant. However, the current demonstrated a steady increase above a turn-on voltage of roughly 1.4 V together with a series resistance of 100 K. Different transports inside the device are responsible for this behavior. The dark *J–V* characteristics are significant for evaluating the electrical characteristics of diodes and determining the heterojunction parameters. As shown in Fig. 10a, *J–V* measurements were used to assess the essential properties of the **APPQ**-based heterojunction. The rectification ratio at a bias voltage of 1.5 V and temperature of 300 K was approximately 120.

Table 9 Total static dipole moment (μ), mean polarizability ($<\alpha>$), anisotropy of the polarizability (Δα), mean first-order hyperpolarizability ($<\beta>$), and second order hyperpolarizability ($<\gamma>$), for **APPQ** using DFT/B3LYP and CAM-B3LYP/6–311+ + G (d, p)

Dipole moment (μ)	PNA	B3LYP	CAM-B3LYP
μ_x, D		−0.3978	−0.3768
μ_y, D		−1.2810	−1.2510
μ_z, D		−0.7926	−0.7566
μ, Debye[a]	2.44 Debye[a]	1.5580	1.5370
polarizability ($<\alpha>$)			
α_{XX}, a.u		−113.0292	−111.03
α_{XY}, a.u		−16.4642	−14.624
α_{YY}, a.u		−161.8898	−159.99
α_{ZZ}, a.u		−163.9981	−160.89
α_{YZ}, a.u		−3.0697	−3.2297
α_{XZ}, a.u		1.0497	1.0557
$<\alpha> \times 10^{-24}$ esu	22×10^{-24} esu[b]	52.1417	46.8904
$\Delta\alpha \times 10^{-24}$ esu		65.6541	57.2560

First-order hyperpolarizability ($<\beta>$)	PNA	B3LYP	CAM-B3LYP
β_{xxx}, a.u		42.2648	40.4268
β_{xxy}, a.u		−7.1203	−6.2123
β_{xyy}, a.u		−28.680	−27.755
β_{yyy}, a.u		−11.811	−10.651
β_{xxz}, a.u		−18.873	−16.783
β_{xyz}, a.u		−22.199	−20.919
β_{yyz}, a.u		−5.2085	−4.5825
β_{xzz}, a.u		21.1897	19.8197
β_{yzz}, a.u		3.4098	2.4908
β_{zzz}, a.u		6.4863	5.8463
$<\beta> \times 10^{-33}$ esu	15.5×10^{-30} esu[c]	35.5213	15.8237
DR		0.5580	0.5050
β_{HRS}		68.4240	62.3210

Second-order hyperpolarizability ($<\gamma>$)	PNA	B3LYP	CAM-B3LYP
γ_{xxxx}, a.u		−14,649.7	−14,468.5
γ_{yyyy}, a.u		−2419.62	−2327.72
γ_{zzzz}, a.u		−505.194	−410.124
γ_{xxyy}, a.u		−3156.67	−3065.54
γ_{xxzz}, a.u		−3020.34	−2825.43
γ_{yyzz}, a.u		−505.893	−499.983
$<\gamma>$ a.u		−3717.3	−3565.3
$<\gamma> \times 10^{-38}$ esu	1.271×10^{-35} esu[d]	-4.8173×10^{-35} esu	-2.0375×10^{-35} esu

a, b, c, d PNA results are taken from references (Kafka et al. 2013; Vishnupriya et al. 2013; Al-Otaibi et al. 2015; Szafran et al. 2007)

Table 10 Calculated thermodynamic parameters of **APPQ**

Parameters	B3LYP/6-311++G (d,p)	CAM/B3LYP/6-311++G(d,p)	HF/6-311++G(d,p)
Zero-point vibrational Energy (kcal/mol)	217. 09471	178.90704	191.24474
Rotational temperature (K)	0.02430	0.01828	0.01817
	0.00374	0.00699	0.00697
	0.00334	0.00608	0.00606
Rotational constant (*GHZ*)			
X	0.50634	0.38082	0.37856
Y	0.07796	0.14595	0.14537
Z	0.06961	0.12670	0.12606
Total energy E_{total}(kcal/mol)	231.523	194.339	206.246
Translational	0.889	0.889	0.889
Rotational	0.889	0.889	0.889
Vibrational	229.745	192.561	204.469

The loaded current–voltage characteristics of the **APPQ**-based heterojunction under illumination of 80 mW/cm^2 are shown in Fig. 10b. When the solar device is illuminated, the *J–V* curve is shifted down by the amount of photocurrent generated. The shifting of *J–V* curves in the fourth quadrant represents that the cell is a generator of electricity. From Fig. 10b, the fourth quadrant part is extracted for obtaining the solar cell parameters. The photocurrent at zero bias (J_{sc}), which represents the short-circuit current density, was calculated and found to be 5.05×10^{-4} A. The voltage at zero current, or the open-circuit voltage V_{oc}, was measured to be 0.62 V. The *J–V* curves were affected significantly by varying the illumination intensity, proving that the **APPQ** /n-Si heterojunction is a strong candidate for photovoltaic and photodetector applications. The output power of the heterojunction can also be calculated as a function of the potential and was found to be 0.225 mW/cm^2. The electron–hole pairs created by the incident light can improve the photovoltaic
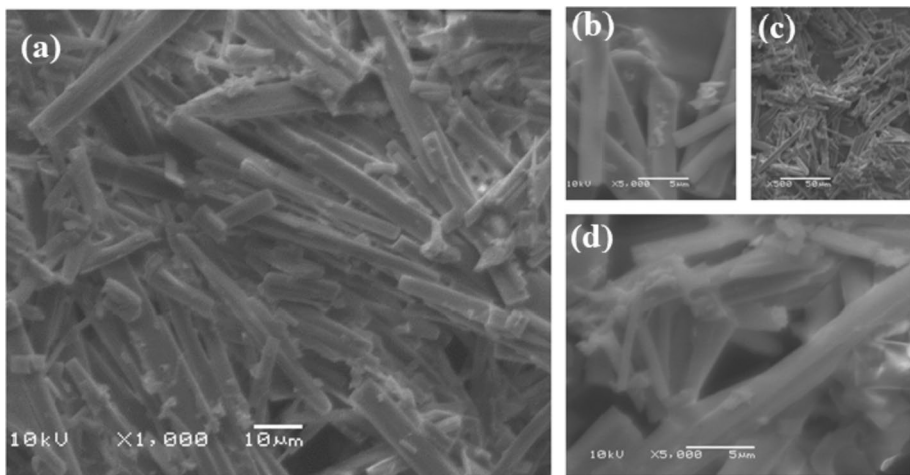
Fig. 6 SEM image for the surface morphology of various magnifications of **APPQ**

Fig. 7 Spectral dependence of Photoluminescence of **APPQ** thin films
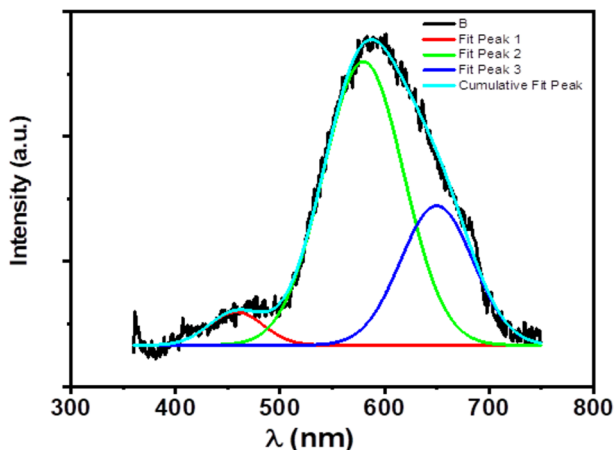
properties. This remarkable device setup additionally promoted the distinctive photovoltaic properties of **APPQ**-based devices.

Furthermore, the obtained photovoltaic parameters in our study were consistent with those documented by Zouhair et al. (2019), A. Aboulouard et al. (2021), Hachi et al. (2018), and Mandal et al. (2020). The calculated value was also assessed to explore the potential applications of the material in photovoltaics. Hence, the photovoltaic parameters collectively indicate the potential utilization of the **APPQ**/n-Si heterojunction as a photovoltaic device. This is attributed to the feasible electron injection process between **APPQ** and n-Si, along with subsequent regeneration, rendering it suitable for photovoltaic applications.

4 Conclusion

In summary, DFT was used to analyze the novel structure **APPQ**, which was created when substrate **1** reacted with phenylhydrazine. The optimized geometrical parameters including bond lengths, bond angles, and dihedral angles were calculated and compared with experimental data. Theoretical values for the ^{1}H and ^{13}C chemical shifts were also calculated and were found to be in very good agreement with the experimental results. The computations of the electronic properties including the UV–Vis spectra and electron transitions were compared with the experimental findings. The initial hyperpolarizability of **APPQ** is greater than most organic structures, a typical NLO material, making it a promising candidate for nonlinear optical applications. All theoretical results were in good agreement with the actual data, and the thermodynamic parameters and electronic absorption characteristics of the molecule were also obtained. An indirect allowed transition with an energy gap of 2.3 eV was observed in the **APPQ** absorption spectra. Based on the dark *I–V* characteristics of **APPQ**, thin films of heterojunction devices may exhibit good rectification properties. Compared to the majority of heterojunctions based on organic materials, the photovoltaic characteristics have a high V_{oc} of 0.62 V and acceptable output power. The results show that **APPQ**-based nanostructured devices can be used in solar cell applications.
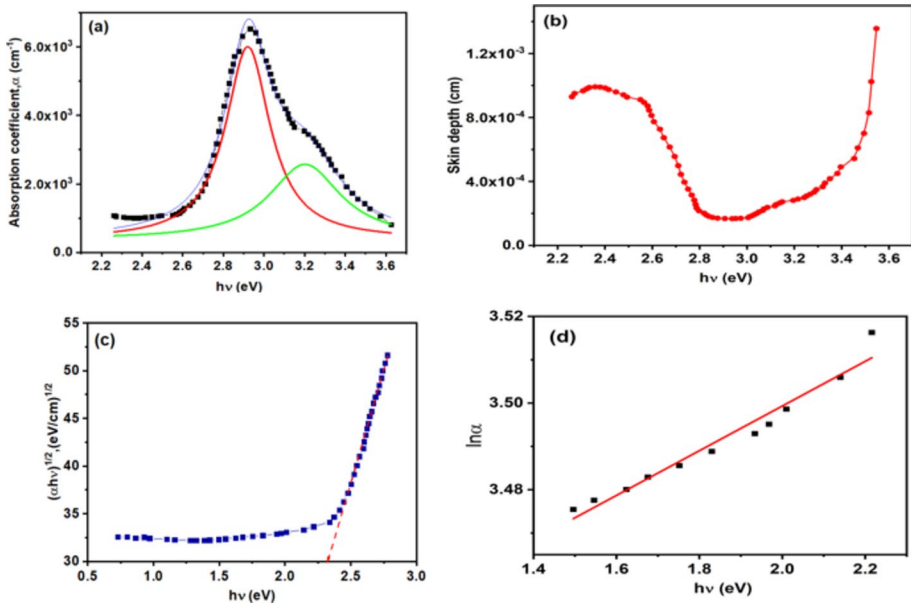
Fig. 8 Plot of photon energy dependence of **a** Absorption coefficient, **b** Skin depth, **c** $(\alpha h\nu)^{1/2}$ of **APPQ** thin films
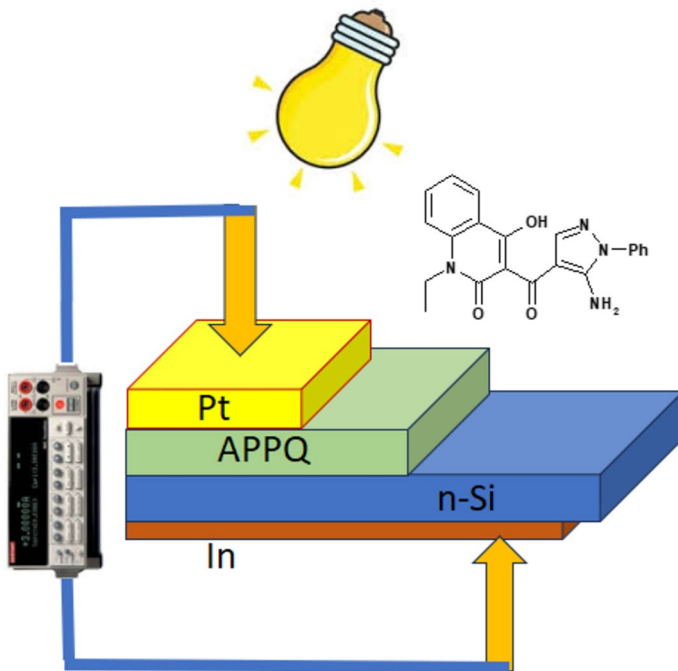
Fig. 9 Schematic illustration of Au/ EHQPP/ n-Si/In heterojunction
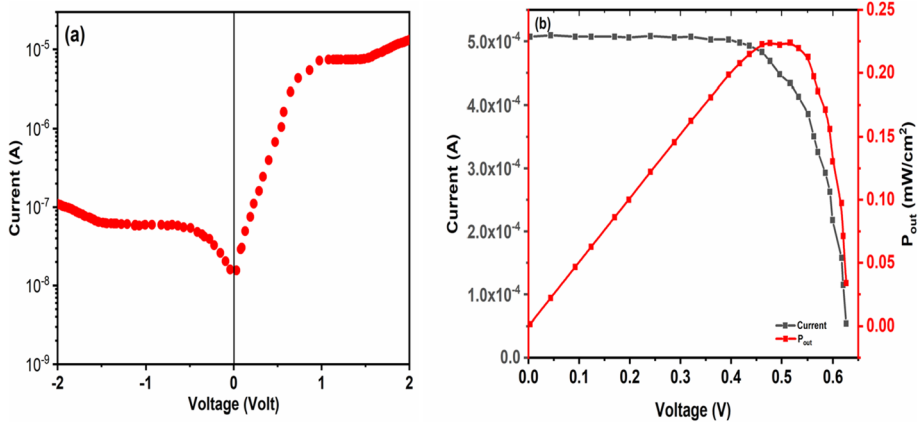
Fig. 10 a Dark J–V characteristics, **b** Loaded J–V characteristics under illumination of 80 mW/cm^2 of **APPQ**–based heterojunction

Availability of data and materials All of the material is owned by the authors and/or no permissions are required.

Declarations

Conflict of interest The authors declare that they have no known competing financial interests or personal relationships that could have appeared to influence the work reported in this paper.

Ethical approval This declaration is "not applicable".

References

Abdel Halim, S., Ibrahim, M.A.: Synthesis, DFT calculations, electronic structure, electronic absorption spectra, natural bond orbital (NBO) and nonlinear optical (NLO) analysis of the novel 5-methyl-8H-benzo[*h*]chromeno[2,3-*b*][1,6]naphthyridine-6(5*H*),8-dione (MBCND). J. Mol. Struct. **1130**, 543–558 (2017)

Abdel Halim, S., Ibrahim, M.A.: Synthesis, DFT calculations, electronic structure, electronic absorption spectra, natural bond orbital (NBO) and nonlinear optical (NLO) analysis of the novel 5-methyl-8*H*-benzo[*h*]chromeno[2,3-*b*][1,6] naphthyridine-6(5H),8-dione (MBCND). J. Mol. Struct. **1130**, 543–558 (2017b)

Abdel Halim, S., Badran, A., Roushdy, N., Ahmed, E.M., Ibrahim, M.A., Farag, A.A.M.: A new hybrid structure based pyranoquinoline-pyridine derivative: synthesis, optical properties, theoretical analysis, and photodiode applications. J. Mol. Struct. **1293**, 136233 (2023)

Abdul Mumit, M., Pal, T.K., Alam, A., Islam, A.-A., Paul, S., Sheikh, C.: DFT studies on vibrational and electronic spectra, HOMO–LUMO, MEP, HOMA, NBO and molecular docking analysis of benzyl-3-N-(2,4,5-trimethoxyphenylmethylene) hydrazinecarbodithioate. J. Mol. Struct. **1220**, 128715 (2020)

Aboulouard, A., Mtougui, S., Demir, N., Moubarik, A., M. E. idrissi, M. Can,: New non-fullerene electron acceptors-based on quinoxaline derivatives for organic photovoltaic cells: DFT computational study. Synth. Met. **279**, 116846 (2021)

Akram, M., Siddique, S.A., Iqbal, J., Hussain, R., Yasir Mehboob, M., Bilal, M., Siddique, A., Naveed, S., Ali, B., Hanif, A., Sajid, M., Shaukat, S.: End-capped engineering of bipolar diketopyrrolopyrrole based small electron acceptor molecules for high performance organic solar cells. Comput. Theor. Chem. **1201**, 113242 (2021)

Almotiri, R.A., Alkhamisi, M.M., Wassel, A.R., El-Mahalawy, A.M.: Optical dispersion and photovoltaic performance of safranin thin films solar cells in hybrid organic-inorganic isotype heterojunction configuration. Mater. Res. Bull. **151**, 111824 (2022)

Al-Otaibi, J.S., Al-Wabli, R.I.: Vibrational spectroscopic investigation (FT-IR and FT-Raman) using ab initio (HF) and DFT (B3LYP) calculations of 3-ethoxymethyl-1, 4-dihydroquinolin-4-one. Spectrochim. Acta Part A Mol. Biomol. Spectrosc. **137**, 7–15 (2015)

Ans, M., Iqbal, J., Muhammad, B.E., Saif, J., Ayub, K.: Opto-electronic properties of non-fullerene fused-undecacyclic electron acceptors for organic solar cells. J. Comput. Mater. Sci. **159**, 150–159 (2019a)

Ans, M., Ayub, K., Muhammad, S., Iqbal, J.: Development of fullerene free acceptors molecules for organic solar cells: a step way forward toward efficient organic solar cells. J. Comptc. **1161**, 26–38 (2019b)

Ans, M., Ayub, K., Bhattia, I.A., Iqbal, J.: Designing indacenodithiophene based non-fullerene acceptors with a donor–acceptor combined bridge for organic solar cells. RSC Adv. **9**, 3605 (2019c)

Ans, M., Iqbal, J., Eliasson, B., Saif, M.J., Javed, H.M.A., Ayub, K.: Designing of non-fullerene 3D star-shaped acceptors for organic solar cells. J. Mol. Mod. **25**, 129 (2019d)

Ans, M., Iqbal, J., Bhattia, I.A., Ayub, K.: Designing dithienonaphthalene based acceptor materials with promising photovoltaic parameters for organic solar cells. RSC Adv. **9**, 34496 (2019e)

Ans, M., Paramasivam, M., Ayub, K., Ludwig, R., Zahid, M., Xiao, X., Iqbal, J.: Designing alkoxy-induced based high performance near infrared sensitive small molecule acceptors for organic solar cells. J. Mol. Liq. **305**, 112829 (2020a)

Ans, M., Ayub, K., Xiao, X., Iqbal, J.: Tuning opto-electronic properties of alkoxy-induced based electron acceptors in infrared region for high performance organic solar cells. J. Mol. Liq. **298**, 111963 (2020b)

Ans, M., Ayub, A., Alwadai, N., Rasool, A., Zahid, M., Iqbal, J., Al-Buriahi, M.S.: Simultaneously enhanced efficiency of eco-friendly structural characterization of the dithienocyclopentacarbazole donor based acceptors with narrow bandgap for high-performance organic solar cells. J. Phys. D Appl. Phys. **55**, 235501 (2022)

Asghari, S., Ramezani, S., Mohseni, M.: Synthesis and antibacterial activity of ethyl 2-amino-6-methyl-5-oxo-4-aryl-5,6-dihydro-4H-pyrano[3,2-c]quinoline-3-carboxylate. Chin. Chem. Lett. **25**, 431–434 (2014)

Cheng, L.T., Tam, W., Stevenson, S.H., Meredith, G.R., Rikken, G., Marder, S.R.: Experimental investigations of organic molecular nonlinear optical polarizabilities. 1. Methods and results on benzene and stilbene derivatives. J. Phys. Chem. **95**, 10631–10643 (1991)

Chernyshev, A.V., Soloveva, E.V., Rostovtseva, I.A., Voloshin, N.A., Demidov, O.P., Shepelenko, K.E., Metelitsa, A.V.: Photo-and ionochromic properties of new spirobenzochromene-pyranoquinoline. Mendeleev Commun. **32**, 531–533 (2022)

El Jouad, Z., Cattin, L., Addou, M., Bernède, J.C., Nunzi, J.-M., Bennacer, R., El Ganaoui, M., El Jouad Bernède, M.: Open circuit voltage of organic photovoltaic cells using C_{60} as acceptor: variation with the donor. Eur. Phys. J. Appl. Phys. **86**, 20201 (2019)

El-Mahalawy, A.M., Almotiri, R.A., Alkhamisi, M.M., Wassel, A.R.: On the optoelectronic performance of solution-processable *N*-(4-methoxy-2-nitrophenyl) acetamide microrods thin films for efficient light detection applications. Surf. Interfaces **30**, 101953 (2022)

Farag, A.A.M., Ibrahim, M.A., El-Gohary, N.M., Roushdy, N.: Synthesis, and photoelectrical characterizations of ECPPQT for optoelectronic application. Arab. J. Chem. **12**, 3723–3731 (2019a)

Farag, A.A.M., Ibrahim, M.A., El-Gohary, N.M., Roushdy, N.: Synthesis, and photoelectrical characterizations of ECPPQT for optoelectronic application. Arab. J. Chem. **12**, 3723–3731 (2019b)

Farag, A.A.M., Abdel Halim, S., Roushdy, N., Badran, A., Ibrahim, M.A.: Facile synthesis and photodetection characteristics of novel nanostructured triazinyliminomethylpyrano[3,2-c]quinoline-based hybrid heterojunction. J. Mol. Struct. **1221**, 128868 (2020)

Frisch, M.J., Trucks, G.W., Schlegel, H.B., Scuseria, G.E., Robb, M.A., Cheeseman, J.R., Scalmani, G., Barone, V., Mennucci, B., Petersson, G.A., Nakatsuji, H., Caricato, M., Li X., Hratchian, H.P., Izmaylov, A.F., Bloino, J., Zheng, G., Sonnenberg, J.L., Hada, M., Ehara, M., Toyota, K., Fukuda, R., Hasegawa, J., Ishida, M., Nakajima, T., Honda, Y., KitA, O., Nakai, H., Vreven, T., Montgomery Jr. J.A., Peralta, J.E., Ogliaro, F., Bearpark, M., Heyd, J.J., Brothers, E., Kudin, K.N., Staroverov, V.N., Kobayashi, R., Normand, J., Raghavachari, K., Rendell, A., Burant, J.C., Iyengar, S.S., Tomasi, J., Cossi, M., Rega, N., Millam, J.M., Klene, M., Knox, J.E., Cross, J.B., Bakken, V., Adamo, C., Jaramillo, J., Gomperts, R., Stratmann, R.E., Yazyev, O., Austin, A.J., Cammi, R., Pomelli, C., Ochterski, J.W., Martin, R.L., Morokuma, K., Zakrzewski,V.G., Voth, G.A., Salvador, P., Dannenberg, J.J., Dapprich, S., Daniels, A.D., Farkas, O., Foresman, J.B., Ortiz, J.V., Cioslowski, J., Fox, D.J.: Gaussian Inc., *Wallingford, CT*, (2009)

Frisch, E., Hratchian H.P., Dennington II R.D., Keith, T.A., Millam, J., Nielsen, A.B., Holder, A.J., Hiscocks J.: Gaussian, Inc., *GaussView Version* 5.0.8, (2009)

Govindarajan, M., Periandy, S., Carthigayen, K.: FT-IR and FT-Raman spectra, thermo dynamical behavior, HOMO and LUMO, UV, NLO properties, computed frequency estimation analysis and electronic structure calculations on abromotoluene. Spectrochim. Acta Part A Mol. Biomol. Spectrosc. **97**, 411–422 (2012)

Hachi, M., Khattabi, S.E., Fitri, A., Benjelloun, A.T., Benzakour, M., Mcharfi, M., Hamidi, M.M.: Bouachrine FT and TD-DFT studies of the pi-bridge influence on the photovoltaic properties of dyes based on thieno[2,3-b]indole. J. Mater. Environ. Sci. **9**(4), 1200–1211 (2018)

Hassanien, A.S., Akl, A.A.: Effect of Se addition on optical and electrical properties of chalcogenide CdSSe thin films. Superlattices Microstruct. **89**, 153–169 (2016)

Hussain, S., Hussain, R., Mehboob, M.Y., Mehboob, M.Y., Chatha, S.A.S., Hussain, A.I., Umar, A., Khan, M.U., Ahmed, M., Adnan, M., Ayub, K.: Adsorption of phosgene gas on pristine and copper-decorated B12N12 nanocages: a comparative DFT study. ACS Omega **5**, 7641–7650 (2020)

Hussein, A.H.M., Gad-Elkareem, M.A.M., El-Adasy, A.A.M., Khames, A.A., Othman, I.M.M.: β-oxoanilides in heterocyclic synthesis: synthesis and antimicrobial activity of pyridines, pyrans, pyrimidines and azolo, azinopyrimidines incorporating antipyrine moiety, inter. J. Org. Chem. **2**, 341–351 (2012)

Ibrahim, M.A., Hassanin, H.M., Abass, M., Badran, S.: Substituted quinolinones. Part 23. Synthesis of 6-ethyl-4, 5-dioxo-5, 6-dihydro-4H-pyrano [3, 2-c] quinoline-3-carboxaldehyde and its chemical behavior towards hydroxylamine hydrochloride. ARKIVOC **4**, 424–431 (2013)

Kafka, S., Pevec, A., Proisl, K., Kimmel, R., Kosmrlj, J.: 4-Hydroxy-1-methyl-3-phenylquinolin-2(1H)-one. Acta Cryst. E **69**, 231–232 (2013)

Kantevari, S., Yempala, T., Surineni, G., Sridhar, B., Yogeeswari, P., Sriram, D.: Synthesis and antitubercular evaluation of novel dibenzo[*b*, d]furan and 9-methyl-9H-carbazole derived hexahydro-2H-pyrano[3,2-c]quinolines *via* Povarov reaction. Eur. J. Med. Chem. **46**, 4827–4833 (2011)

Karabacak, M.: the spectroscopic (FT-IR and FT-Raman) and theoretical studies of 5-bromo-salicylic acid. J. Mol. Struct. **919**, 215–222 (2009)

Lee, C.T., Yang, W.T., Parr, R.G.B.: Development of the Colle-Salvetti correlation-energy formula into a functional of the electron density. Phys. Rev. **37**, 785–790 (1988)

Li, B., Sun, Z., Zhai, Y., Jiang, J., Huang, Y., Meng, J.: Rapid decoloration and acidichromism of photochromic 3,3-diaryl-3*h*-pyrano[3,2-*f*]quinolines. Tetrahedron **75**, 130471 (2019)

Liu, L., Alam, M.S., Lee, D.-U.: Synthesis, antioxidant activity and fluorescenceproperties of novel europium complexes with (E)-2- or 4-hydroxy-N'-[(2- hydroxynaphthalen-1 yl)methylene]benzohydrazide Schiff base. Bull. Korean Chem. Soc. **33**(10), 3361–3367 (2012)

Mandal, S., Kandregula, G.R., Tokala, V.N.B.: A computational investigation of the influence of acceptor moieties on photovoltaic performances and adsorption onto the TiO_2 surface in triphenylamine-based dyes for DSSC application. J. Photochem. Photobiol. A Chem. **401**, 112745 (2020)

Maynard, A.T., Huang, M., Rice, W.G., Covell, D.G.: Reactivity of the HIV-1 nucleocapsid protein p7 zinc finger domains from the perspective of densityfunctional theory. Proc. Natl. Acad. Sci. u.s.a. **95**, 11578–11583 (1998)

Mehboob, M.Y., Hussain, R., Khan, M.U., Adnan, M., Umar, A., Alvi, M.U., Ahmed, M., Khalid, M., Iqbal, J., Akhtar, M.N., Zafar, F., Shahi, M.N.: Designing N-phenylaniline-triazole configured donor materials with promising optoelectronic properties for high-efficiency solar cells. J. Comput. Chem. **1186**, 112908 (2020)

Mehboob, M.Y., Khan, M.U., Hussain, R., Ayub, K., Sattar, A., Ahmad, M.K., Saira, Z.I., Adnan, M.: Designing of benzodithiophene core-based small molecular acceptors for efficient non-fullerene organic solar cells. Spectrochim. Acta A **244**, 118873 (2021)

Mehboob, M.Y., Zaier, R., Hussain, R., Adnan, M., Asif Iqbal, M.M., Irshad, Z., Bilal, I., Janjua, M.R.S.A.: In silico modeling of acceptor materials by end-capped and π-linker modifications for high-performance organic solar cells: estimated PCE > 18%. Comput. Theor. Chem. **1208**, 113555–113565 (2022)

Mehboob, M.Y., Hussain, R., Adnan, M., Saira, A., Farwa, U., Irshad, Z., Ramzan, M., Ashraf Janjua, S.: Theoretical modelling of novel indandione-based donor molecules for organic solar cell applications. J. Phy. Chem. Solids **162**, 110508–110518 (2022a)

Mehboob, M.Y., Hussain, R., Khan, M.U., Adnan, M., Alvi, M.U., Yaqoob, J., Khalid, M.: Efficient designing of half-moon-shaped chalcogen heterocycles as non-fullerene acceptors for organic solar cells. J. Mol. Mod. **28**, 125 (2022b)

Mostafa, M.A., Ismail, M. M., Morsy, J. M., Hassanin, H. M., Abdelrazek, M. M., Synthesis, characterization, anticancer, and antioxidant activities of chitosan Schif bases bearing quinolinone or pyranoquinolinone and their silver nanoparticles derivatives, Polymer Bulletin **80**, 4035–4059 (2023)

Pauling, L.: The nature of the chemical bond and the structure of molecules and crystals: an introduction to modern structural chemistry, 3rd edn. Cornell University Press, New York (1960)

Petersson, D.A., Allaham, M.A.: A complete basis set model chemistry. II. open-shell systems and the total energies of the first-row atoms. J. Chem. Phys. **94**, 6081–6090 (1991)

Roeges, N.P.G.: A Guide to the Complete Interpretation of Infrared Spectra of Organic Structures. Wiley, New York (1994)

Romdhane, A., Jannet, H.B.: Synthesis of new pyran and pyranoquinoline derivatives. Arab. J. Chem. **10**, S3128–S3134 (2017)

Roushdy, N., Badran, A., Abdel Halim, S., Farag, A.A.M., Ibrahim, M.A.: Production, optical characterization and DFT analysis of a nanofiber structure of a new pyridinylcarbonylquinoline: synthesis and photovoltaic application. J. Mol. Struct. **1270**, 133846 (2022)

Safari, J., Zarnegar, Z., Heydarian, M.: Magnetic Fe_3O_4 nanoparticles as efficient and reusable catalyst for the green synthesis of 2-amino-4*H*-chromene in aqueous media. Bull. Chem. Soc. Jpn **85**, 1332–1338 (2012)

Sarafran, M., Komasa, A., Adamska, E.B.: Molecular structure, vibrational spectroscopic (FT-IR, FT-Raman), UV and NBO analysis of 2-chlorobenzonitrile by density functional method. J. Mol. Struct. **827**, 101–107 (2007)

Shahab, S., Kumar, R., Darroudi, M., Borzehandani, M.Y.: Molecular structure and spectroscopic investigation of sodium (*E*)-2-hydroxy-5-((4-sulfonatophenyl) diazenyl) benzoate: a DFT study. J. Mol. Struct. **1083**, 198–203 (2015)

Siddique, M.B.A., Hussain, R., Siddique, S.A., Mehboob, M.Y., Irshad, Z., Iqbal, J., Adnan, M.: Designing triphenylamine configured donor materials with promising photovoltaic propertiesfor highly efficient organic solar cells. Chem. Sel. **5**, 7358–7369 (2020)

Siddique, S.A., Naveed, S., Alvi, M.U., Mehboob, M.Y., Ali, B., Rauf, A., Siddique, M.B.A., Hussain, R., Arshad, M., Liu, X.: Deciphering the role of end-capped acceptor units for amplifying the photovoltaic properties of donor materials for high-performance organic solar cell applications. Comput. Theor. Chem. **1205**, 113454 (2021a)

Siddique, S.A., Arshad, M., Naveed, S., Mehboob, M.Y., Adnan, M., Hussain, R., Ali, B., Siddique, M.B.A., Liu, X.: Efficient tuning of zinc phthalocyanine-based dyes for dye-sensitized solar cells: a detailed DFT study. RSC Adv. **11**, 27570 (2021b)

Siddique, S.A., Altaf, S., Ahmed, E., Naveed, S., Siddique, M.B.A., Hussain, R., Liu, X., Rauf, A., Arshad, M.: Discovery of versatile bat-shaped acceptor materials for high-performance organic solar cells—a DFT approach. Int. J. Energy Res. **46**, 13393–13408 (2022)

Soliman, H.N., Yahia, I.S.: Synthesis and technical analysis of 6-butyl-3-[(4-chlorophenyl)diazenyl]-4-hydroxy-2H-pyrano[3,2-c]quinoline-2,5(6H)-dione as a new organic semiconductor: Structural, optical and electronic properties. Dyes Pig. **176**, 108199 (2020)

Szafran, M., Komasa, A., Bartoszak-Adamska, E.: Crystal and molecular structure of 4-carboxypiperidinium chloride (4-piperidinecarboxylic acid hydrochloride). J. Mol. Struct. **827**, 101–107 (2007)

Tauc, J., Menth, A.: States in the gap. J. Non-Cryst. Solids **8**, 569–585 (1972)

Upadhyay, K.D., Shah, A.K.: Evaluation of pyrano[3,2-c]quinoline analogues as anticancer agents. Anti-Cancer Agents Med. Chem. **19**, 1285–1292 (2019)

Uppal, J., Mir, P.A., Chawla, A., Kumar, N., Kaur, G., Bedi, P.M.S., Bhandari, D.D.: Pyranoquinolone derivatives: a potent multi-targeted pharmacological scaffold. J. Heterocycl. Chem. **60**, 369–391 (2023)

Urbach, F.: The long-wavelength edge of photographic sensitivity and of the electronic absorption of solids. Phys. Rev. **92**, 1324–1324 (1953)

Vishnupriya, R., Suresh, J., Sivakumar, S., Kumar, R.R., Lakshman, P.L.N.: 4-(4-fluorophenyl)-6-methylamino-5-nitro-2-phenyl-4h-pyran-3-carbonitrile. Acta Cryst. E **69**, 687–688 (2013)

Wang, T., Liu, J., Zhong, H., Chen, H., Lv, Z., Zhang, Y., Zhang, M., Geng, D., Niu, C., Li, Y., Li, K.: Synthesis and antitumor activity of novel ethyl 3-aryl-4-oxo-3,3a,4,6-tetrahydro-1H-furo[3,4-c]pyran-3a-carboxylates. Bioorg. Med. Chem. Lett. **21**, 3381 (2011)

Wolinski, K., Hinton, J.F., Pulay, P.: Efficient implementation of the gauge-independent atomic orbital method for NMR chemical shift calculations. J. Am. Chem. Soc. **112**, 8251–8260 (1990)

Yanai, T., Tew, D., Handy, N.: A new hybrid exchange–correlation functional using the Coulomb-attenuating method (CAM-B3LYP). Chem. Phys. Lett. **393**, 51–57 (2004)

Yousef, T.A., Abu El-Reash, G.M., El Morshedy, R.M.: Quantum chemical calculations, experimental investigations, and DNA studies on (E)-2-((3- hydroxynaphthalen-2-yl)methylene)-N-(pyridin-2-yl) hydrazinecarbothioamide and its Mn(II) Ni(II), Cu(II), Zn(II) and Cd(II) complexes. Polyhedron **45**(1), 71–85 (2012)

Zaman, A.-Z., Ahmad, I., Pervaiz, M., Ahmad, S., Kiran, S., Khan, M.A., Gulzar, T., Kamal, T.: A novel synthetic approach for the synthesis of pyrano[3,2-c]quinolone-3-carbaldehydes by using modified Vilsmeier Haack reaction, as potent antimicrobial agents. J. Mol. Struct. **1180**, 227–236 (2019)

Zhang, R., Dub, B., Sun, G., Sun, Y.: Experimental and theoretical studies on o-, m- and p-chlorobenzylideneaminoantipyrines. Spectrochim. Acta A **75**, 1115–1124 (2010)

Authors and Affiliations

Magdy A. Ibrahim[1] · Al-Shimaa Badran[1] · Shimaa Abdel Halim[1] · N. Roushdy[2] · A. A. M. Farag[3]

✉ A. A. M. Farag
alaafaragg@gmail.com

Magdy A. Ibrahim
magdy_ahmed1977@yahoo.com

Al-Shimaa Badran
badran.shimaa@yahoo.com

Shimaa Abdel Halim
shimaaquantum@ymail.com

[1] Chemistry Department, Faculty of Education, Ain Shams University, Roxy, Cairo 11711, Egypt

[2] Electronics Materials Department, Advanced Technology and New Materials Research Institute, City of Scientific Research and Technological Applications (SRTA-City), New Borg El-Arab City, Alexandria 21934, Egypt

[3] Thin-Film Laboratory, Physics Department, Faculty of Education, Ain Shams University, Roxy, Cairo 11711, Egypt